Aleix Casals Cheng

Lévy flights for competition avoidance in microbial dynamics

Bachelor's Degree in Engineering Mathematics and Physics

Final Degree Project

Directed by
Dr. Àlex Arenas Moreno

UNIVERSITAT ROVIRA i VIRGILI

Tarragona, 6 June 2025

To all the walkers, whether real or simulated, who venture far enough to uncover something new.

Acknowledgements

I would like to express my deepest gratitude to Dr. Àlex Arenas for his invaluable support, guidance, and patience throughout the development of this project.

His insights and encouragement were essential to its completion. I especially appreciate the time he always took to listen to my doubts, ensure I was on the right path, and for the engaging and thoughtful conversations that made the whole process more enriching.

Abstract

This project explores how Lévy flights influence competitive dynamics in biological systems through theoretical analysis and numerical simulations. We examine two key scenarios: one-dimensional foraging efficiency, where performance strongly depends on both the movement strategy and the metric used to assess it, and two-dimensional spatial dynamics, where single-species systems exhibit clustering and pattern formation driven by local interactions.

Building on these foundations, we analyze the competition between two species with different movement strategies through R-based visualizations. We find that motility differences lead to spatial segregation and, in some cases, emergent oscillatory dynamics qualitatively resembling predator-prey cycles, despite the absence of direct predation.

Resum

Aquest projecte explora com els vols de Lévy influeixen en la dinàmica competitiva dels sistemes biològics mitjançant anàlisi teòrica i simulacions numèriques. Examinem dos escenaris clau: l'eficiència de cerca en una dimensió, on el rendiment depèn tant de l'estratègia de moviment com del mètode utilitzat per avaluar-la, i la dinàmica espacial en dues dimensions, on sistemes d'una sola espècie mostren agregació i formació de patrons causats per interaccions locals.

A partir d'aquestes bases, analitzem la competència entre dues espècies amb estratègies de moviment diferents utilitzant visualitzacions fetes amb R. Observem que les diferències en la motilitat condueixen a una segregació espacial i, en alguns casos, a dinàmiques oscil·lants emergents que qualitativament recorden cicles depredador-presa, tot i l'absència de predació directa.

Resumen

Este proyecto explora cómo los vuelos de Lévy influyen en la dinámica competitiva de los sistemas biológicos mediante análisis teórico y simulaciones numéricas. Se examinan dos escenarios clave: la eficiencia de búsqueda en una dimensión, donde el rendimiento depende tanto de la estrategia de movimiento como del criterio utilizado para evaluarla, y la dinámica espacial en dos dimensiones, donde sistemas de una sola especie presentan agrupamiento y formación de patrones impulsados por interacciones locales.

Sobre estas bases, se analiza la competencia entre dos especies con estrategias de movimiento distintas mediante visualizaciones realizadas en R. Se observa que las diferencias en la motilidad conducen a una segregación espacial y, en algunos casos, a dinámicas oscilatorias emergentes que recuerdan cualitativamente ciclos depredador-presa, a pesar de la ausencia de depredación directa.

Keywords: Lévy flights, foraging efficiency, species competition, spatial dynamics, motility regulation, pattern formation, R simulations, statistics.

Contents

List of Figures

Chapter 1

Introduction

1.1 Context

Foraging, the act of searching for resources like food, is a fundamental behavior seen across many animal species. Although animals can move freely, their strategies are constrained by biological needs and environmental conditions, such as the necessity to find food within a limited time. Evolution has shaped foraging behaviors to optimize energy gain relative to effort, often leading to surprisingly efficient movement patterns.

Interestingly, similar search behaviors appear beyond biology, such as in human activities like criminal investigations [6] and internet browsing [5]. Efficient search is therefore a concept relevant not only in ecology, but also in areas of human behavior and information foraging.

One of the main tools for modeling search behavior is the random walk, which assumes movement as a series of random steps. Traditional models often use random walks with well-defined mean and variance, which simplifies analysis but may not always reflect real-world behavior. Observations in nature suggest that many organisms exhibit movement patterns that include rare, long-distance steps, something not well captured by standard models.

Lévy flights offer a powerful alternative. These are random walks where long steps are more probable, following a power-law distribution that may lack a defined mean or variance. This makes them well-suited for modeling irregular movement patterns that include both short steps and occasional very long relocations, as seen in real foragers.

Beyond individual movement, an important ecological question is how interactions between individuals, such as competition for shared resources, shape collective behavior. Spatial pat-

terns and clustering can emerge from these interactions, especially in microbial communities where localized competition, motility, and resource consumption give rise to dynamic structures. Understanding how movement strategies like Lévy flights influence these emergent spatial distributions is crucial for explaining how species coexist, avoid direct competition, or dominate a shared environment.

1.2 Objective

The goal of this project is to investigate how Lévy flight movement strategies influence species competition in two-dimensional environments. We focus on understanding how differences in motility and competition types give rise to spatial patterns, clustering, and segregation, ultimately affecting species coexistence and dominance.

1.3 Methodology

The project is divided into two main parts: theoretical analysis and numerical simulations.

We begin by studying the theoretical foundations of Lévy flights, exploring how they differ from traditional random walks. This includes examining their probability distributions, conditions under which statistical moments are defined, and how the exponent parameter μ shapes movement characteristics.

Next, we implement numerical simulations in one dimension. We study Lévy flights with absorbing boundaries to validate how foraging efficiency depends on the exponent μ. We consider both destructive and nondestructive foraging modes and emphasize how different efficiency estimators can produce varying outcomes, affecting how performance is evaluated.

The two-dimensional simulations form the core of this project. We first examine a single-species scenario to investigate how spatial patterns and clusters emerge solely from local interactions and movement strategies. This foundational step clarifies the role of Lévy flights in pattern formation. Building on this, we introduce competition between two species with distinct movement strategies, analyzing how these differences influence spatial organization, competitive advantage, and resource access. All simulations were performed in R, with a strong focus on visualizing spatial distributions and cluster dynamics to aid interpretation. The full set of codes and scripts is available here [1].

Chapter 2

Theoretical Background

Before exploring how Lévy walks relate to foraging behavior, we first examine their basic properties and mathematical background. This chapter introduces the main ideas and theoretical framework behind Lévy random walks.

2.1 Random Walks

Random walks describe processes driven by chance and unpredictability. They can explain movements as small as a pollen grain shaking under a microscope or as large as the ups and downs of a financial market. In each case, what appears as disorderly wandering actually follows simple probabilistic rules.

Formally, a one-dimensional random walk is a mathematical process that describes the position of a walker as it takes steps along a line. The position after n steps is denoted by X_n, and it is given by the sum of all individual steps taken up to that point:

$$X_n = \sum_{i=1}^{n} \ell_i,$$

where each ℓ_i represents the step taken at time i. These steps are independent and identically distributed random variables drawn from a probability distribution $p(\ell)$. The choice of this probability distribution determines the behavior of the walk. For example, whether the steps are small and frequent, or occasionally large.
To understand the properties of random walks, we often analyze the **moments** of the step lengths ℓ_i. The 1st moment is the **mean**, which represents the average step length, while the 2nd moment is related to the **variance**, which measures the spread or variability of the step lengths.

Now, we classify random walks based on their step length distributions, which are characterized by these moments [6]:

- **Brownian random walk**: in this type of random walk, the steps ℓ_i are typically small and drawn from a distribution that has a well-defined mean and variance. This means that the 1st moment (mean) and the 2nd moment of the step distribution are finite. In this case, the overall path becomes smoother over time. A common example is when the step lengths follow a Gaussian (normal) distribution.

- **Lévy random walk**: in this type of walk, step lengths follow a heavy-tailed distribution, often a power law. Depending on the exponent, the mean or variance of step lengths may be infinite. This leads to movement patterns with many short steps and some very long jumps, creating irregular paths.

This foundational framework of random walks, where each step is drawn from a probability distribution, provides the basis for more complex processes. In the next section, we will rigorously explore the mathematical structure of Lévy random walks (also known as Lévy flights) and how different values of the characteristic exponent μ impact on the walk's properties.

2.2 Lévy Flights

Lévy flights are a class of random walks characterized by step lengths that follow a heavy-tailed probability density function. Specifically, each step of length ℓ is drawn from a probability density function (P.D.F) of the form

$$p(\ell) \sim \ell^{-\mu}. \tag{2.1}$$

As discussed in [6], these random walks are classified as Lévy flights only when the exponent satisfies $1 < \mu \leq 3$. This regime is particularly interesting because it implies the presence of occasional very long jumps, which significantly affect the statistical and dynamical properties of the process.

Now, we will explore the mathematical properties of Lévy flights, focusing on the existence of the normalization constant, first and second moments.

To begin our analysis, we note that the probability density function is not well-defined at $\ell = 0$ due to the divergence of the power-law behavior. Consequently, we introduce a lower cutoff $\ell_{\min} > 0$ and consider step lengths in the domain $\ell \in [\ell_{\min}, +\infty)$, with all steps being positive. This restriction avoids the singularity at the origin.

2.2.1 Characterization of the Lévy Flights PDF

We begin by deriving the normalization constant for the Lévy flight probability density function (PDF), ensuring that the total probability integrates to one. The derivations of the first and second moments, which follow a similar approach, are provided in the Annex A.1 for completeness.

To obtain the normalization constant, we evaluate the following integral and determine under which conditions a well-defined constant $C \in \mathbb{R}$ exists.

- For $\mu > 1$

$$\begin{aligned}
\int_{\ell_{\min}}^{+\infty} p(l)\, dl &= \int_{\ell_{\min}}^{+\infty} C \cdot l^{-\mu}\, dl = 1 \\
&\Rightarrow \int_{\ell_{\min}}^{+\infty} C \cdot l^{-\mu}\, dl = C \int_{\ell_{\min}}^{+\infty} l^{-\mu}\, dl \\
&= C\, \frac{l^{1-\mu}}{1-\mu}\bigg|_{\ell_{\min}}^{+\infty} = C \left(\lim_{l \to +\infty} \frac{l^{1-\mu}}{1-\mu} - \frac{\ell_{\min}^{1-\mu}}{1-\mu} \right) \\
&= C \cdot \frac{\ell_{\min}^{1-\mu}}{\mu - 1} = 1 \Rightarrow \boxed{C = \frac{\mu - 1}{\ell_{\min}^{1-\mu}}}
\end{aligned} \tag{2.2}$$

  In the evaluation of the anti-derivative, the term at the upper limit is

$$\lim_{l \to +\infty} \frac{l^{1-\mu}}{1-\mu} = 0$$

  Since $\mu > 1 \to 1 - \mu < 0$ in this range, we are taking the limit of a negative power of l, which vanishes as $l \to +\infty$. Therefore, the integral converges and the normalization is valid.

- For $\mu = 1$

$$\begin{aligned}
\int_{\ell_{\min}}^{+\infty} p(l)\, dl &= \int_{\ell_{\min}}^{+\infty} C \cdot l^{-1}\, dl = 1 \\
&\Rightarrow \int_{\ell_{\min}}^{+\infty} C \cdot l^{-1}\, dl = C \int_{\ell_{\min}}^{+\infty} \frac{1}{l}\, dl \\
&= C \ln(l)|_{\ell_{\min}}^{+\infty} = C \left(\lim_{l \to +\infty} \ln(l) - \ln(\ell_{\min}) \right) \\
&= C \cdot (+\infty - \ln(\ell_{\min})) = +\infty
\end{aligned}$$

As we can see, the integral diverges for $\mu = 1$ due to the logarithmic term growing without bound. This means that the probability density function is not normalizable in this case, i.e., there is no constant C that satisfies

$$\int_{\ell_{\min}}^{+\infty} C \cdot l^{-1}\, dl = 1.$$

Therefore, $\mu = 1$ does not define a valid Lévy flight distribution, as the total probability cannot be properly constrained.

- For $\mu < 1$

$$\begin{aligned}
\int_{\ell_{\min}}^{+\infty} p(l)\, dl = \int_{\ell_{\min}}^{+\infty} C \cdot l^{-\mu}\, dl = 1 \\
\Rightarrow \int_{\ell_{\min}}^{+\infty} C \cdot l^{-\mu}\, dl = C \int_{\ell_{\min}}^{+\infty} l^{-\mu}\, dl \\
= C\, \frac{l^{1-\mu}}{1-\mu}\bigg|_{\ell_{\min}}^{+\infty} \\
= C \left(\lim_{l \to +\infty} \frac{l^{1-\mu}}{1-\mu} - \frac{\ell_{\min}^{1-\mu}}{1-\mu} \right) \\
= C \left(+\infty - \frac{\ell_{\min}^{1-\mu}}{1-\mu} \right) = +\infty
\end{aligned}$$

Again, the integral diverges for $\mu < 1$ because in this regime the exponent $1 - \mu > 0$, so $l^{1-\mu}$ grows without bound as $l \to +\infty$. As a result, the normalization condition cannot be satisfied.

We conclude that, for the Lévy distribution to define a valid probability density function (PDF), it is necessary that $\mu > 1$.

Summarizing the behavior of the Lévy flight PDF for different values of μ, we find in Annex A.1 that its statistical properties are characterized as follows:

$$p(\ell) = \begin{cases} \text{Not normalizable (divergent total probability)} & \text{if } \mu \leq 1, \\ \text{Undefined first and second moments (both diverge)} & \text{if } 1 < \mu \leq 2, \\ \text{Finite first moment, but divergent second moment} & \text{if } 2 < \mu \leq 3, \\ \text{Finite first and second moments (Brownian behavior)} & \text{if } \mu > 3. \end{cases}$$

Therefore, according to equation (2.1), genuine Lévy flight behavior occurs in the range $1 < \mu \leq 3$.

2.2.2 Cumulative Distribution Function for Lévy Flights

Another useful representation of a probability distribution is its **cumulative distribution function** (CDF). The CDF, denoted $P(\ell)$, gives the probability that a step length is less than or equal to a given value ℓ:

$$P(\ell) = \mathbb{P}(l \leq \ell) = \int_{\ell_{\min}}^{\ell} p(l)\, dl$$

Substituting the power-law form of $p(\ell)$ for $\mu > 1$, we get:

$$P(\ell) = \int_{\ell_{\min}}^{\ell} C \cdot l^{-\mu}\, dl = C\, \frac{l^{1-\mu}}{1-\mu}\bigg|_{\ell_{\min}}^{\ell} = \frac{C}{1-\mu} \cdot (\ell^{1-\mu} - \ell_{\min}^{1-\mu})$$

Substituting the expression for C from Equation 2.2 into the CDF, we obtain:

$$P(\ell) = \frac{\mu - 1}{\ell_{\min}^{1-\mu}(1-\mu)} \left(\ell^{1-\mu} - \ell_{\min}^{1-\mu}\right) = \frac{\mu - 1}{\ell_{\min}^{1-\mu}(\mu-1)} \left(\ell_{\min}^{1-\mu} - \ell^{1-\mu}\right) = 1 - \left(\frac{\ell}{\ell_{\min}}\right)^{1-\mu} \tag{2.3}$$

It is useful to observe that this cumulative distribution function is invertible. Since we will later require its inverse, we derive it here:

$$P(P^{-1}(u)) = 1 - \left(\frac{P^{-1}(u)}{\ell_{\min}}\right)^{1-\mu} = u \quad \Longrightarrow \quad \left(P^{-1}(u)\right)^{1-\mu} = (1-u)\, \ell_{\min}^{1-\mu}$$
$$\Longrightarrow \boxed{P^{-1}(u) = \ell_{\min} \cdot (1-u)^{1/(1-\mu)}} \tag{2.4}$$

With all of this in mind, we are now able to model a foraging process using Lévy random walks.

Chapter 3

Idealized Model of Foraging

We will study an idealized model presented by [6] that capture some of the essential dynamics of foraging in the limit case where predator-pray relationships are ignored. So we will have the simple case where we have a forager searching for target sites that will be randomly distributed. The forager behaves as follows:

1. When a target lies within a "direct vision" range r_v, the forager detects it with a given probability and moves straight toward that target.

2. If no target is detected within the radius r_v, the forager randomly selects a direction and a step length ℓ_j sampled from the distribution given by equation (2.1). It then moves incrementally along this path, continuously scanning within radius r_v for any targets. If no target is found during the movement, the forager stops after traveling the distance ℓ_j and then repeats the process by choosing a new direction and step length ℓ_{j+1}. If a target is detected along the way, the forager immediately proceeds directly to it as described in the first rule.

Furthermore, to evaluate whether a searching strategy is effective, we define the search efficiency, η, as

$$\eta = \frac{\text{Number of visited target sites}}{\text{Total distance traversed by the forager}} \tag{3.1}$$

In order to study this efficiency from a theoretical perspective, it is necessary to work with expected values. For this reason, we introduce the mean number of steps N that a forager takes between two consecutive target sites. This allows us to analytically relate the search efficiency to the statistical properties of the movement.

Assuming the forager takes a total of $S > 0$ steps during its search, we have:

- Number of visited target sites: $\frac{S}{N}$
- Total distance traveled by the forager: $S \cdot < \ell >$

Therefore:

$$\eta = \frac{\frac{S}{N}}{S \cdot < \ell >} = \frac{1}{N \cdot < \ell >} \tag{3.2}$$

So now we will obtain the expressions for N and $< \ell >$.

On one hand, we need to find an expression for the mean number of steps taken by a forager between two successive target sites. The value of N can be found analytically in the 1D case [6], when the Lévy flight starts from a point s in the interval $[0, L]$ with absorbing boundaries. This means the walker stops when it reaches position 0 or position L, which here means it reached a target site. To do this, we assume the forager cannot detect a target while it is within the direct vision range r_v, and only detects it exactly when on the target. With these assumptions, the average number of steps before absorption is given by:

$$N = K\left(\frac{s(L-s)}{r_v^2}\right)^{(\mu-1)/2} \tag{3.3}$$

where the constant K does not depend on s, and L. The full derivation of this formula lies beyond the scope of this project. However, we demonstrate in appendix A.2 that, in the specific case of a Brownian random walk where all steps have a fixed length r_v (corresponding to $\mu > 3$), the resulting expression is $N = s(L-s)r_v^{-2}$.

On the other hand, we will start off by assuming for simplicity that $l_{min} = r_v$. This restriction may have biological motivation, since it is unreasonable for the forager to change the direction of the flight within the distance of the direct vision from the previous turning point.

Then, for 1D Lévy random walk we already have the expression $< \ell > = C \cdot \frac{r_v^{2-\mu}}{\mu-2} = r_v \cdot \frac{\mu-1}{\mu-2}$ with $\mu > 2$, but we would also like to study the search efficiency for $1 < \mu \leq 2$.
To do an estimation of the search efficiency behavior in 1D, let $\lambda > 0$ be the mean free path of the forager between successive target sites. Then, by assuming that **distances between successive target sites are identically equal to** λ, so there are no flights longer than λ:

$$
\begin{aligned}
< \ell > &= \int_{r_v}^{+\infty} l \cdot p(l) dl = \int_{r_v}^{+\infty} l \cdot C \cdot l^{-\mu} dl = \int_{r_v}^{\lambda} l \cdot C \cdot l^{-\mu} dl + \int_{\lambda}^{+\infty} l \cdot C \cdot l^{-\mu} dl \\
&\approx \int_{r_v}^{\lambda} l \cdot C \cdot l^{-\mu} dl + \int_{\lambda}^{+\infty} \lambda \cdot C \cdot l^{-\mu} dl = C\left(\int_{r_v}^{\lambda} l^{1-\mu} dl + \lambda \int_{\lambda}^{+\infty} l^{-\mu} dl \right) \\
&= C\left(\frac{l^{2-\mu}}{2-\mu}\Big|_{r_v}^{\lambda} + \lambda \frac{l^{1-\mu}}{1-\mu}\Big|_{\lambda}^{+\infty} \right) = C\left(\frac{\lambda^{2-\mu} - r_v^{2-\mu}}{2-\mu} - \lambda \frac{\lambda^{1-\mu}}{1-\mu} \right) \\
&= \frac{\mu - 1}{r_v^{1-\mu}} \left(\frac{\lambda^{2-\mu} - r_v^{2-\mu}}{2-\mu} + \frac{\lambda^{2-\mu}}{\mu - 1} \right) = \boxed{\left(\frac{\mu - 1}{2-\mu} \right) \left(\frac{\lambda^{2-\mu} - r_v^{2-\mu}}{r_v^{1-\mu}} \right) + \frac{\lambda^{2-\mu}}{r_v^{1-\mu}}}
\end{aligned}
\tag{3.4}
$$

To further study the search efficiency, we will define two types of foraging strategies: destructive and nondestructive foraging. From this point onward, all mathematical derivations in this section will assume that the distances between successive target sites are identically equal to λ.

3.1 Destructive Foraging

Destructive foraging happens when the target site found by the forager becomes undetectable in all subsequent flights. This occurs when the target site is "eaten" or destroyed by the foraging animal. So the walker will start on a destroyed site which is about λ distance away from the two remaining sites. Therefore, following Figure 3.1 we can adapt the problem by assigning $s = L - s = \lambda$.

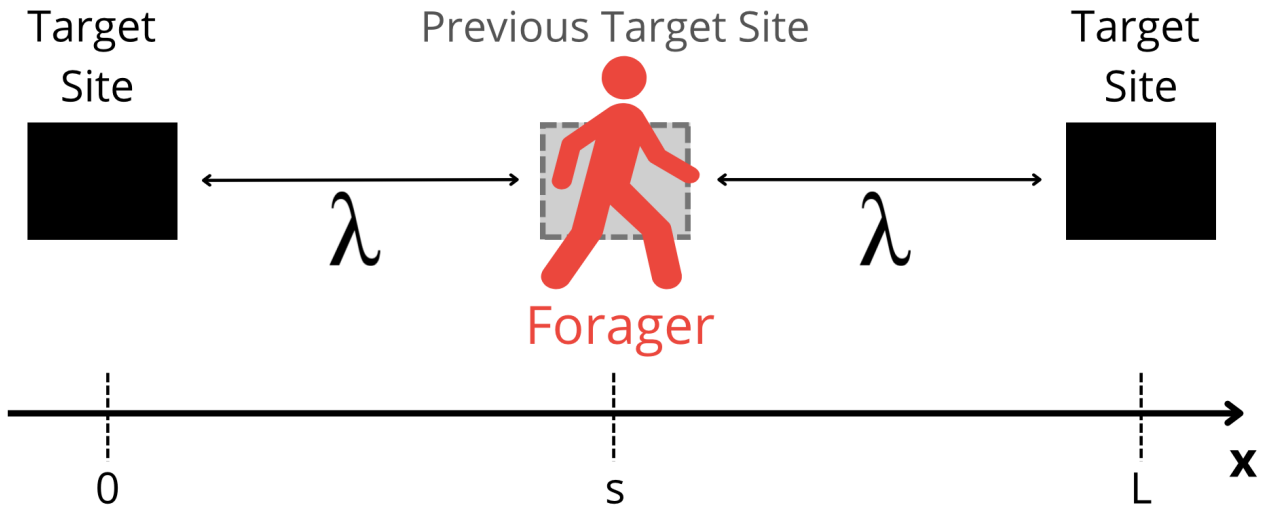

Figure 3.1: Scheme for destructive foraging. We can see starting point $s = \lambda$ and target sites at 0 and $L = 2\lambda$.

Hence, the average number of steps taken by the walker before it is absorbed from equation 3.3 on destructive foraging (we will denote it as N_d) is:

$$N_d = K\left(\frac{s(L-s)}{r_v^2}\right)^{(\mu-1)/2} = K\left(\frac{\lambda^2}{r_v^2}\right)^{(\mu-1)/2} = K\left(\frac{\lambda}{r_v}\right)^{\mu-1} \tag{3.5}$$

Using equations 3.2, 3.4, and 3.5, we can now derive and analyze the foraging efficiency analytically denoted as η_d for the destructive foraging. Recall that throughout these theoretical results, we assume that successive target sites are separated by a fixed distance λ.

$$\begin{aligned}\eta_d &= \frac{1}{N_d \cdot <\ell>} = \frac{1}{K\left(\frac{\lambda}{r_v}\right)^{\mu-1} \cdot \left[\left(\frac{\mu-1}{2-\mu}\right)\left(\frac{\lambda^{2-\mu}-r_v^{2-\mu}}{r_v^{1-\mu}}\right) + \frac{\lambda^{2-\mu}}{r_v^{1-\mu}}\right]} \\ &= \frac{1}{K\lambda^{\mu-1} \cdot \left[\left(\frac{\mu-1}{2-\mu}\right)\left(\lambda^{2-\mu} - r_v^{2-\mu}\right) + \lambda^{2-\mu}\right]}\end{aligned} \tag{3.6}$$

To continue with the derivation, we will also assume a *sparsely* distributed target sites, i.e., $\lambda >> r_v$. Then, as $1 < \mu < 2 \rightarrow 2 - \mu > 0$ so we can approximate the following:

$$\begin{aligned}\eta_d &\approx \frac{1}{K\lambda^{\mu-1} \cdot \left[\left(\frac{\mu-1}{2-\mu}\right)\lambda^{2-\mu} + \lambda^{2-\mu}\right]} = \frac{1}{K\lambda \cdot \left[\left(\frac{\mu-1}{2-\mu}\right) + 1\right]} \\ &= \frac{1}{K\lambda \cdot \left[\frac{\mu-1+2-\mu}{2-\mu}\right]} = \boxed{\frac{2-\mu}{K\lambda}}\end{aligned} \tag{3.7}$$

We can see that the search efficiency has no maximum and it is higher for lower μ. So the foraging will be more efficient when μ tends to 1.

To gain more insight into why values of μ close to 1 lead to more efficient foraging, we compute the probability of making steps shorter than λ when $\mu = 1 + \varepsilon$, and take the limit $\varepsilon \rightarrow 0^+$ (since $\mu \leq 1$ is not allowed).

$$\begin{aligned}\lim_{\varepsilon\to 0^+}\mathbb{P}(r_v<\ell<\lambda) &= \lim_{\varepsilon\to 0^+}\int_{r_v}^{\lambda} p(l)dl = \lim_{\varepsilon\to 0^+} C\int_{r_v}^{\lambda} l^{-\mu}dl \\ &= \lim_{\varepsilon\to 0^+}\frac{(\mu-1)}{r_v^{1-\mu}}\frac{l^{1-\mu}}{(1-\mu)}\Big|_{r_v}^{\lambda} = \lim_{\varepsilon\to 0^+}\left(\frac{\mu-1}{1-\mu}\right)\frac{(\lambda^{1-\mu}-r_v^{1-\mu})}{r_v^{1-\mu}} \\ &= \lim_{\varepsilon\to 0^+}\frac{(r_v^{1-\mu}-\lambda^{1-\mu})}{r_v^{1-\mu}} = \lim_{\varepsilon\to 0^+}(r_v^{-\varepsilon}-\lambda^{-\varepsilon})\cdot r_v^{\varepsilon} = 0\end{aligned}$$

We can conclude that as μ gets near to 1 steps lower than λ are negligible (they will mostly not happen). So steps will be λ or higher. Hence, as we assumed that there will be target sites every λ distance, the forager will mainly walk straight lines until a target is spotted. This will indeed have the maximum search efficiency in a 1D domain.

Putting all this together, we obtain the following expression for the search efficiency $\eta_d(\mu)$ in the destructive foraging model, across different Lévy flight regimes:

$$\eta_d(\mu)\approx\begin{cases}\dfrac{2-\mu}{K\lambda} & \text{if } 1<\mu<2,\\[2ex] \dfrac{1}{K\lambda\left[\ln\left(\frac{\lambda}{r_v}\right)+1\right]} & \text{if } \mu=2,\\[2ex] \dfrac{\mu-2}{K\lambda(\mu-1)}\left(\dfrac{r_v}{\lambda}\right)^{\mu-2} & \text{if } 2<\mu\leq 3.\end{cases} \tag{3.8}$$

The derivation of this approximated efficiency expression for the intermediate case $2\leq\mu\leq 3$ can be found in Annex A.3.

It is important to emphasize that the efficiency expression derived above relies on a set of approximations that are most reliable at the boundaries of the interval $1<\mu\leq 3$. In particular:

- For $\mu\to 1^+$, the approximation becomes increasingly accurate, as the probability of taking steps shorter than the target spacing λ becomes negligible. In this regime, the forager essentially performs long, straight movements between targets, matching our assumptions.
- However, in the intermediate region, especially around $\mu=2$, the situation is more subtle. For example, in the regime $1<\mu<2$, we assumed $\left(\frac{\lambda}{r_v}\right)^{2-\mu}\gg 1$ in order to simplify the expression. But as $\mu\to 2$, the exponent $2-\mu$ becomes small, making the quantity $\left(\frac{\lambda}{r_v}\right)^{2-\mu}$ close to 1, rather than significantly greater, which reduces the accuracy of the approximation.

Therefore, while the approximated expression for $\eta_d(\mu)$ in Eq. (3.8) captures the expected qualitative behavior across the Lévy regime, one should be cautious when interpreting its accuracy near $\mu = 2$, where the underlying assumptions become less reliable. A more precise analysis in this region lies beyond the scope of this work.

3.2 Nondestructive Foraging

Nondestructive foraging occurs when the forager can visit the same target site many times. This can happen by having target sites temporally depleted or if the forager becomes satisfied and leaves the site before using all the resources.

Since now we can revisit previous sites, the mean number N_d overestimates the true number of flights between target sites. Therefore we will now define N_{nd} as the mean number of flights between successive sites for the nondestructive foraging. This corresponds when the walker starts at some small distance r_v from a previously visited site and the next one about λ distance away, i.e., $s = r_v$ and $L = \lambda$

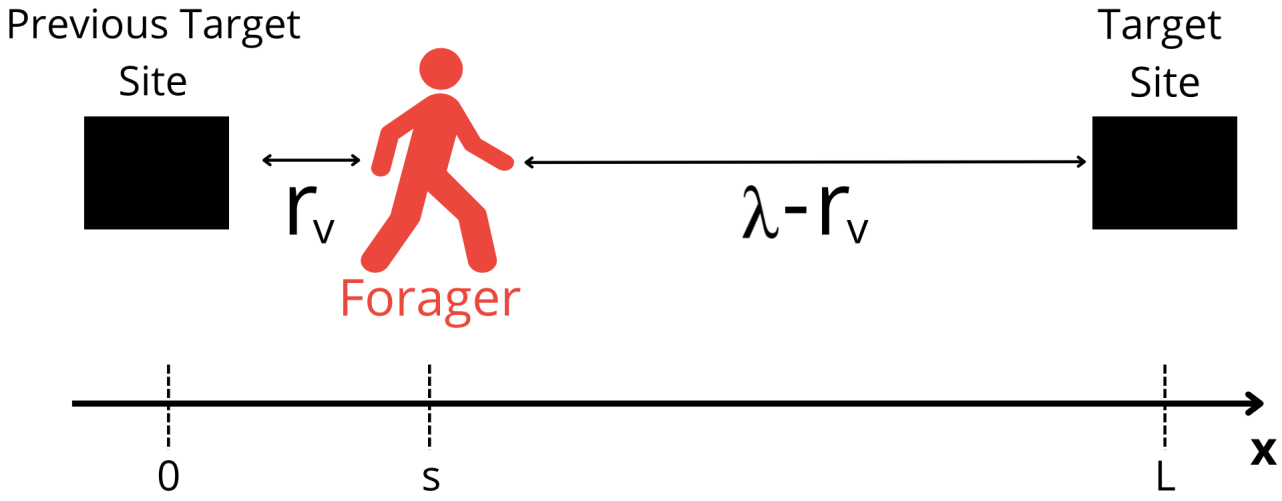

Figure 3.2: Scheme for nondestructive foraging. Starting point $s = r_v$, targets at 0 and $L = \lambda$.

By again assuming a *sparsely* distributed target sites, now we can approximate:

$$N_{nd} = K\left(\frac{s(L-s)}{r_v^2}\right)^{(\mu-1)/2} = K\left(\frac{r_v(\lambda - r_v)}{r_v^2}\right)^{(\mu-1)/2} \approx \boxed{K\left(\frac{\lambda}{r_v}\right)^{(\mu-1)/2}} \tag{3.9}$$

Then, we shall proceed as before to study how will the efficiency, η_{nd} be when $1 < \mu < 2$ case:

$$\begin{aligned}
\eta_{nd} &= \frac{1}{N_{nd} \cdot <\ell>} = \frac{1}{K\left(\frac{\lambda}{r_v}\right)^{(\mu-1)/2} \cdot \left[\left(\frac{\mu-1}{2-\mu}\right)\left(\frac{\lambda^{2-\mu}-r_v^{2-\mu}}{r_v^{1-\mu}}\right) + \frac{\lambda^{2-\mu}}{r_v^{1-\mu}}\right]} \\
&\approx \frac{1}{K\lambda^{(\mu-1)/2}\frac{r_v^{\mu-1}}{r_v^{(\mu-1)/2}} \cdot \left[\left(\frac{\mu-1}{2-\mu}\right)\lambda^{2-\mu} + \lambda^{2-\mu}\right]} \\
&= \frac{1}{K\lambda^{2-\mu}\lambda^{(\mu-1)/2}\frac{r_v^{\mu-1}}{r_v^{(\mu-1)/2}} \cdot \left[\frac{\mu-1}{2-\mu} + 1\right]} = \frac{2-\mu}{K\lambda^{2-\mu+(\mu-1)/2} \cdot r_v^{\mu-1-(\mu-1)/2}} \\
&= \frac{2-\mu}{K\lambda^{1+(1-\mu)/2} \cdot r_v^{(\mu-1)/2}} = \boxed{\frac{(2-\mu)}{K\lambda}\left(\frac{\lambda}{r_v}\right)^{(\mu-1)/2}}
\end{aligned} \tag{3.10}$$

As before, we can now get the approximate efficiency for the nondestructive case:

$$\eta_{nd}(\mu) \approx \begin{cases} \dfrac{2-\mu}{K\lambda} \cdot \left(\dfrac{\lambda}{r_v}\right)^{(\mu-1)/2} & \text{if } 1 < \mu < 2, \\ \dfrac{1}{K\sqrt{\lambda r_v}\left[\ln\left(\frac{\lambda}{r_v}\right) + 1\right]} & \text{if } \mu = 2, \\ \dfrac{\mu-2}{Kr_v(\mu-1)}\left(\dfrac{r_v}{\lambda}\right)^{(\mu-1)/2} & \text{if } 2 < \mu \leq 3. \end{cases} \tag{3.11}$$

The derivation of this approximated efficiency expression for the intermediate case $2 \leq \mu \leq 3$ can be found in Annex A.3.

As a final remark, just like in the destructive case, the efficiency approximation here works best when μ is close to 1 or 3. In the intermediate range, especially near $\mu = 2$, the assumptions used in the derivation become less reliable, so the expression may not be as accurate. A more detailed analysis could give better results in that region, but this goes beyond the scope of this work.

Chapter 4

Numerical Modeling of Lévy Flights in One Dimension

This chapter presents a numerical simulation of 1D Lévy flights, aimed at validating the theoretical results discussed earlier.

4.1 Numerical Setup

In our simulations, step sizes are generated using **inverse transform sampling**. This method uses the inverse of the cumulative distribution function (CDF) of the Lévy distribution (see Eq. (2.4)).

The idea comes from the *Probability Integral Transform* theorem [4], which says:

If a random variable X has CDF F_X, then the new variable

$$Y := F_X(X)$$

follows a uniform distribution on the interval $[0, 1]$.

This means that if we already have a random variable X, we can turn it into a uniform variable using its CDF. We can also do the opposite, starting from a uniform variable and getting a random variable that follows a given distribution.

So in our case, to generate a Lévy-distributed step length ℓ, we do the following:

- Sample a value U from a uniform distribution: $U \sim \mathcal{U}(0, 1)$.

- Use the inverse CDF of the Lévy distribution to get the step size:

$$P(\ell) = U \quad \Longrightarrow \quad \ell = P^{-1}(U)$$

After sampling the step length ℓ, we choose the direction of the step at random. It can be either to the right $(+1)$ or to the left (-1), with equal probability.

The forager moves within a finite interval $[0, L]$ with absorbing boundaries at both ends. Unlike the idealized model in Chapter 3, where the forager stops upon entering the visual range r_v, here it continues moving until absorption. This assumption was already made in the theoretical derivations in that chapter.

4.2 Defining Efficiency Estimators for 1D Lévy Flights

We analyze the efficiency η of Lévy walks introduced in Section 3.1, considering both destructive and nondestructive foraging scenarios. In each simulation, the walker finds exactly one target before stopping. We will now discuss which estimator of efficiency to use, which will determine what quantities we need to measure in the simulations.

Let d be the total distance traveled in a single run. Three natural estimators for efficiency are:

1. $\eta_1 = \frac{1}{\langle d \rangle}$
2. $\eta_2 = \frac{1}{\langle N \rangle \langle \ell \rangle}$
3. $\eta_3 = \left\langle \frac{1}{d} \right\rangle$

At first glance, η_3 appears most faithful to the definition, computing $1/d$ for each run and averaging. However, for Lévy flights, this is unreliable. Because d is heavy-tailed, η_3 can be dominated by rare short runs, even if most are long and inefficient.

To illustrate:

- **Case 1:** 99 runs with $d = 1$, and 1 with $d = 1000$.

$$\eta_3 = \frac{1}{100}(99 \cdot 1 + 1 \cdot \frac{1}{1000}) \approx 0.990, \quad \eta_1 \approx 0.091.$$

- **Case 2:** 99 runs with $d = 1000$, and 1 with $d = 1$.

$$\eta_3 \approx 0.011, \quad \eta_1 \approx 0.001.$$

- **Case 3:** 50 runs with $d = 1$, and 50 with $d = 1000$.

$$\eta_3 \approx 0.501, \quad \eta_1 \approx 0.002.$$

Despite half the runs being inefficient, η_3 suggests 50% efficiency which is misleading.

These examples show that η_3 is overly sensitive to rare, highly efficient runs, while η_1 better reflects the overall behavior of the forager. For this reason, we use η_1 as our main efficiency estimator in simulations.

We also compute η_2 in simulations because it corresponds to the theoretical efficiency expression derived in Chapter 3. Since both $\langle N \rangle$ and $\langle \ell \rangle$ have known analytical forms, η_2 provides a direct link between theory and simulation results.

To relate η_1 and η_2, recall that the total distance traveled is

$$d = \sum_{i=1}^{N} \ell_i,$$

where the steps ℓ_i are independent and identically distributed. We denote by $\bar{\ell} = \frac{1}{N} \sum_{i=1}^{N} \ell_i$ the mean step length in a single run. Taking expectations:

$$\langle d \rangle = \left\langle \sum_{i=1}^{N} \ell_i \right\rangle = \langle N \cdot \bar{\ell} \rangle = \langle \bar{\ell} \rangle \langle N \rangle + \mathrm{Cov}(N, \bar{\ell}).$$

Since $\langle \bar{\ell} \rangle = \langle \ell \rangle$, and assuming N and ℓ are weakly correlated, we approximate

$$\langle d \rangle \approx \langle N \rangle \langle \ell \rangle,$$

which leads to

$$\eta_1 = \frac{1}{\langle d \rangle} \approx \frac{1}{\langle N \rangle \langle \ell \rangle} = \eta_2. \tag{4.1}$$

In practice, when N and ℓ are weakly correlated, as often seen in truncated Lévy walks, η_1 and η_2 remain close. If correlations are stronger (e.g., longer jumps mean fewer steps), the two estimators can differ noticeably.

4.3 Simulation Results for 1D Lévy Flights

Our goal is to understand how efficiency depends on the Lévy exponent μ, and to compare the two efficiency estimators, η_1 and η_2, under both destructive and nondestructive foraging scenarios, as introduced in Chapter 3.

We begin by revisiting the theoretical expressions derived for η_2 in Chapter 3. It is worth noting that the constant K appearing in Eq. (3.3) generally depends on the Lévy exponent μ. However, for simplicity, we treat K as a constant when plotting the theoretical curves. As a result, we do not expect perfect quantitative agreement with simulations. Determining the exact form of $K(\mu)$ is beyond the scope of this work, and our focus remains on qualitative comparison.

We then present simulation results for three different values of the target spacing λ in the destructive case, and four different λ values in the nondestructive case. For each setting, the Lévy exponent μ varies over the range $\mu \in [1.05, 3]$ in steps of 0.05.

Since the theoretical expressions for efficiency scale as $1/\lambda$ in both cases, we plot the rescaled quantity $\lambda\eta$ instead of η itself. This rescaling allows for easier comparison across different values of λ. To distinguish between estimators, we use η_{d1} and η_{d2} for the destructive case, and η_{nd1} and η_{nd2} for the nondestructive case.

4.3.1 Destructive Foraging in 1D Lévy Flights

To interpret the simulation outcomes, we first examine the theoretical predictions for destructive foraging. Figure 4.1(a) displays the estimator η_{d2} derived from Eq. (3.6), along with its approximate form from Eq. (3.8). This comparison provides insight into the expected efficiency behavior across different Lévy exponents μ for $\lambda = 10^3$.

From the plot, we observe that the green curve, representing the approximate expression, begins to deviate noticeably from the exact expression shown by the dashed red line around $\mu = 2$. This highlights the need to use the approximation with caution, as it performs best near the boundaries $\mu \approx 1$ and $\mu \approx 3$.

Having established the theoretical expectations, we now turn to the simulation results for both η_{d1} and η_{d2}, shown in Fig. 4.1 for various values of λ. The two estimators exhibit similar qualitative trends, though differences become more apparent for small μ and large λ.

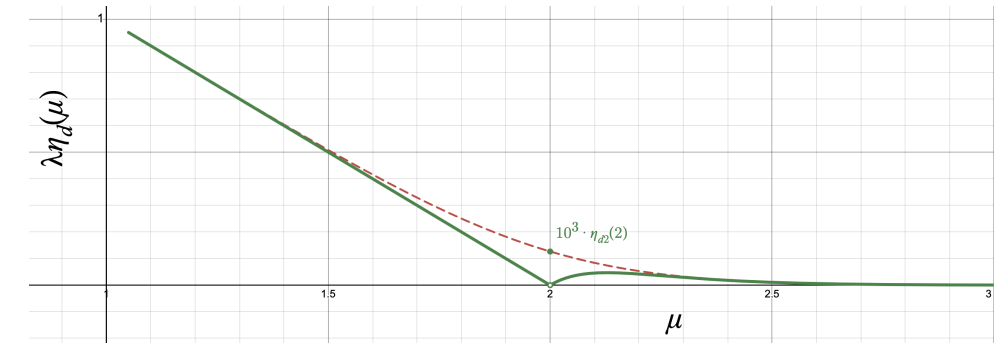

(a) Theoretical estimator η_{d2}

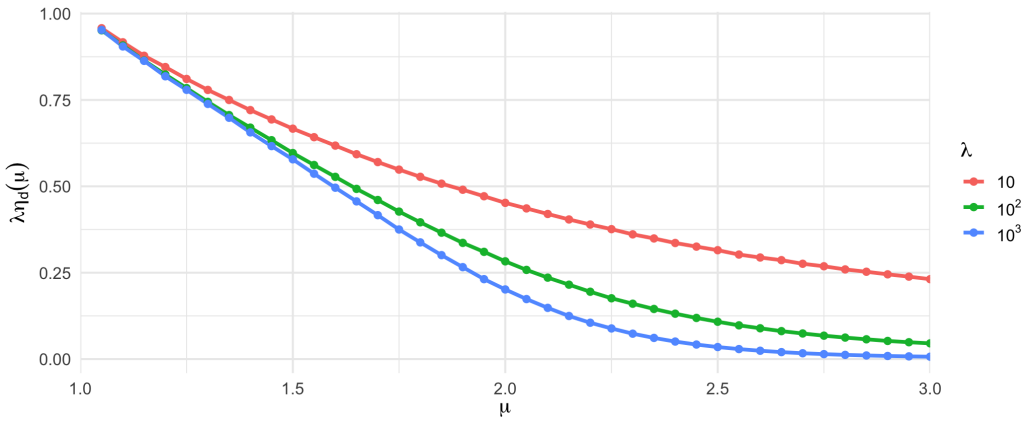

(b) Simulated estimator η_{d1}

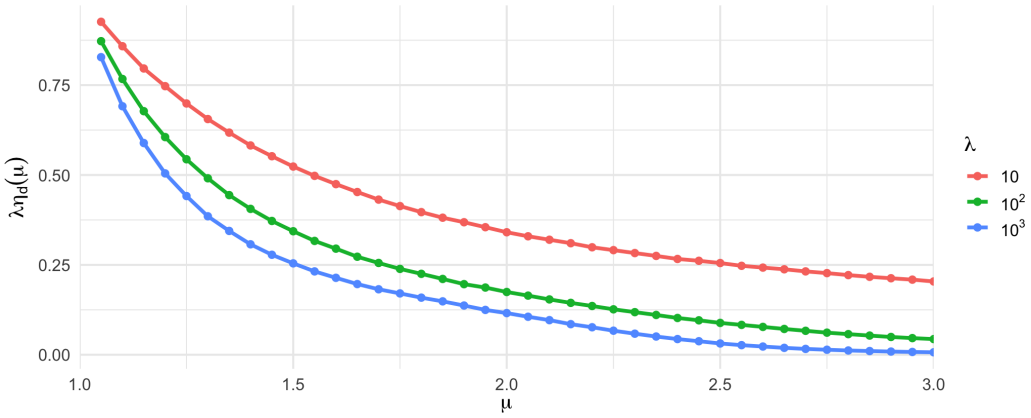

(c) Simulated estimator η_{d2}

Figure 4.1: (a) Theoretical estimator η_{d2} for destructive foraging: the red dashed curve shows the exact expression from Eq. (3.6) for $\lambda = 10^3$, while the green curve shows the approximation from Eq. (3.8). Parameters: $K = 1$, $r_v = 1$. (b) Simulated estimator η_{d1} and (c) simulated estimator η_{d2} for destructive foraging. Differences between estimators are more pronounced for small μ and large λ, but diminish as μ increases.

To quantify their agreement, we compute the relative error plotted in Fig. 4.2:

$$\varepsilon_d = \left| \frac{\eta_{d1} - \eta_{d2}}{\eta_{d1}} \right|$$

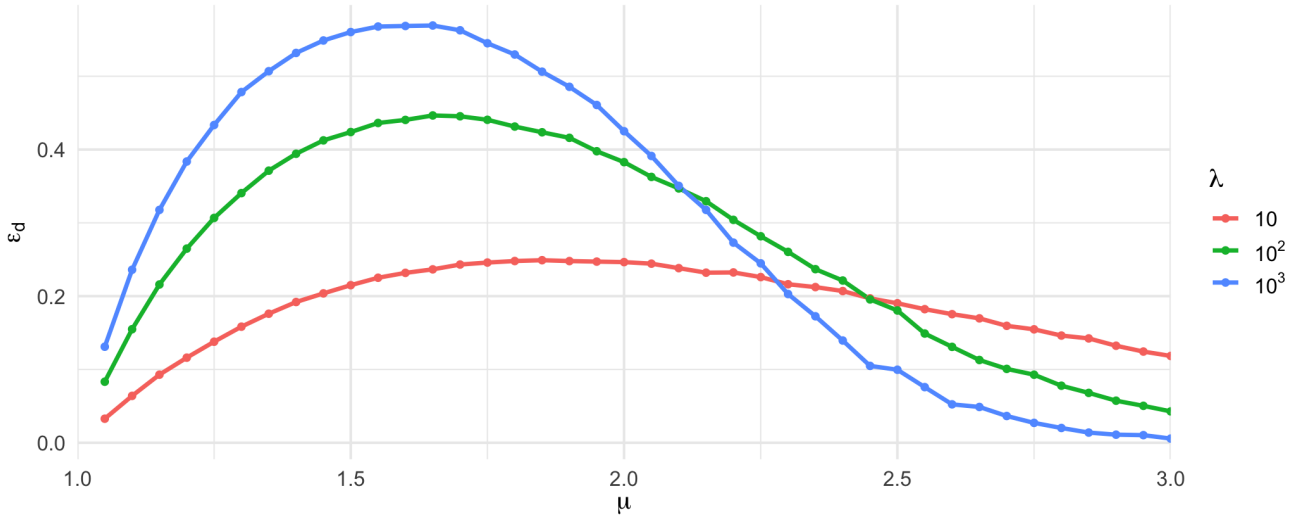

Figure 4.2: Relative error ε_d between η_{d1} and η_{d2} across μ for various λ. The error grows for small μ and large λ.

The largest errors occur in the range $\mu \in (1, 2)$ and increase with λ. To understand this, we examine the Pearson correlation coefficient $\rho(N_d, \bar{\ell})$ between the number of steps N_d and the average step length $\bar{\ell}$ (Fig. 4.3).

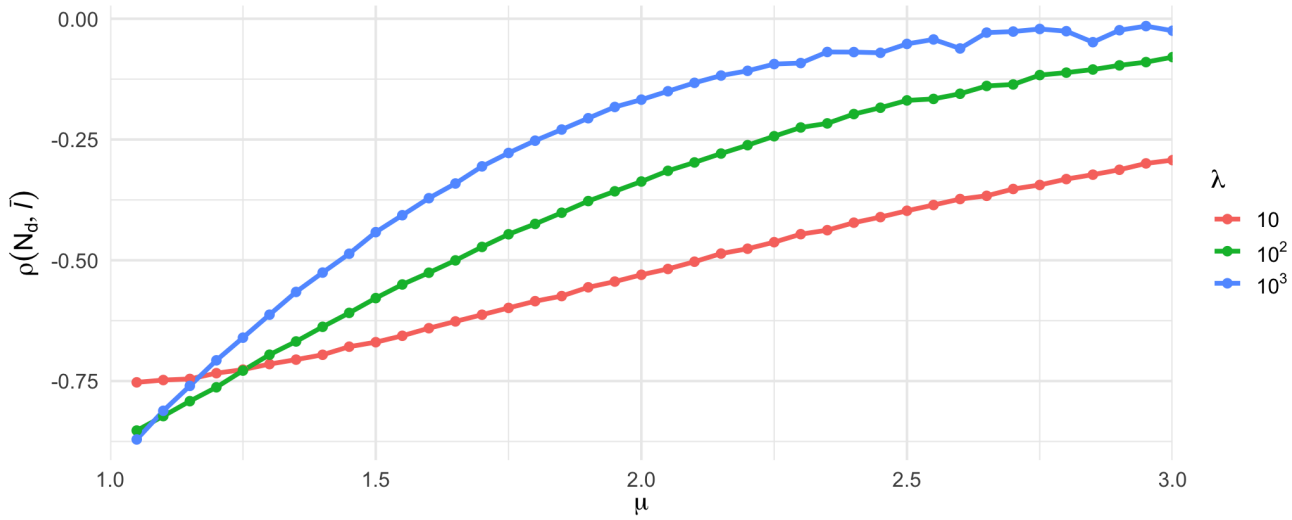

Figure 4.3: Pearson correlation coefficient $\rho(N_d, \bar{\ell})$ as a function of μ and λ. Negative correlation is strongest for small μ and decreases as λ and μ grow.

A pronounced negative correlation is evident for $\mu < 2$, especially at smaller λ. This reflects the intuition that walkers taking longer steps tend to find targets in fewer steps. As λ increases, the correlation weakens, suggesting the independence assumption behind η_{d2} becomes more valid.

Interestingly, while $\rho(N_d, \bar{\ell})$ decreases with λ, the relative error ε_d grows. This apparent contradiction arises because the derivation of η_{d2} relies on neglecting the covariance term in $\langle d \rangle$ as shown in 4.1. Since $\rho(N_d, \bar{\ell})$ is normalized by the standard deviations σ_{N_d} and $\sigma_{\bar{\ell}}$, a small correlation coefficient does not guarantee a negligible covariance. The covariance can still be large enough to affect $\langle d \rangle$ significantly.

To directly assess the magnitude of this effect, we compute the unnormalized covariance $\mathrm{Cov}(N_d, \bar{\ell})$ as shown in Fig. 4.4. We observe that this quantity increases with λ, even as the correlation weakens.

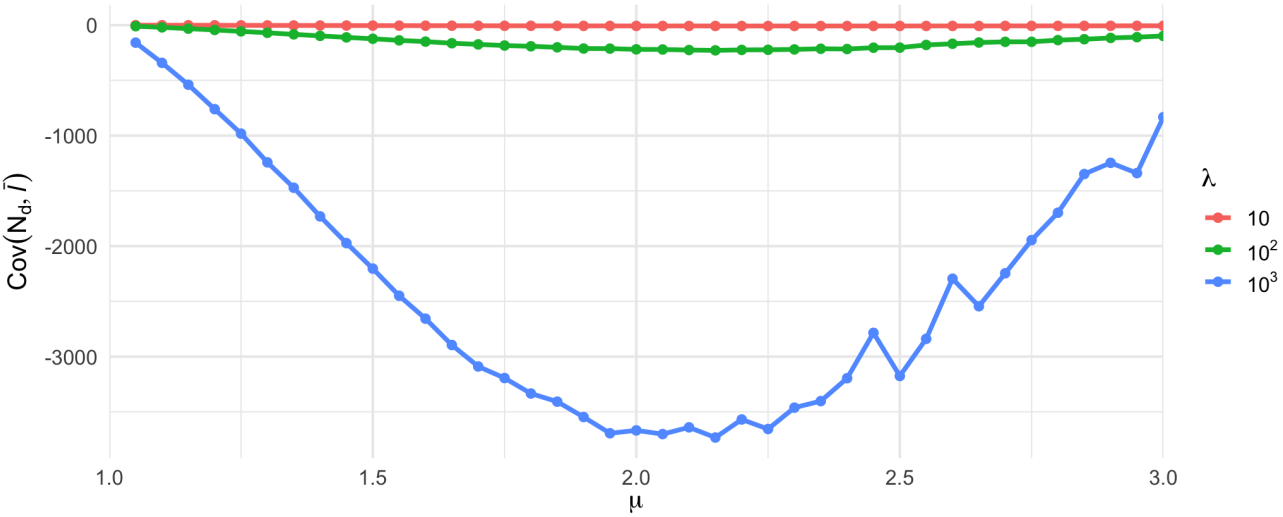

Figure 4.4: Covariance $\mathrm{Cov}(N_d, \bar{\ell})$ versus μ for $\lambda = 10, 10^2, 10^3$, showing significant dependency despite decreasing correlation.

To confirm that incorporating the covariance results in a corrected estimator, we compute:

$$\eta_{d2}^{\mathrm{corr}} = \frac{1}{\langle N_d \rangle \langle \ell \rangle + \mathrm{Cov}(N_d, \bar{\ell})} = \frac{1}{1/\eta_{d2} + \mathrm{Cov}(N_d, \bar{\ell})},$$

which reduces the relative error to negligible levels, as shown in Fig. 4.5. This confirms that the discrepancy between η_{d1} and η_{d2} arises primarily from the covariance term.

In summary, both η_{d1} and η_{d2} can be used to estimate foraging efficiency, but they do not always give the same result. Their difference becomes noticeable when μ is small and λ is large. This happens because η_{d2} assumes that the number of steps and the step length are independent, an assumption that breaks down in these conditions. Even though the correlation between them weakens as λ increases, the actual (unnormalized) covariance can still have a strong effect. Once this covariance is taken into account, the two estimators match closely.

This highlights the importance of being clear about which estimator is used when reporting efficiency, especially in regimes where they differ.

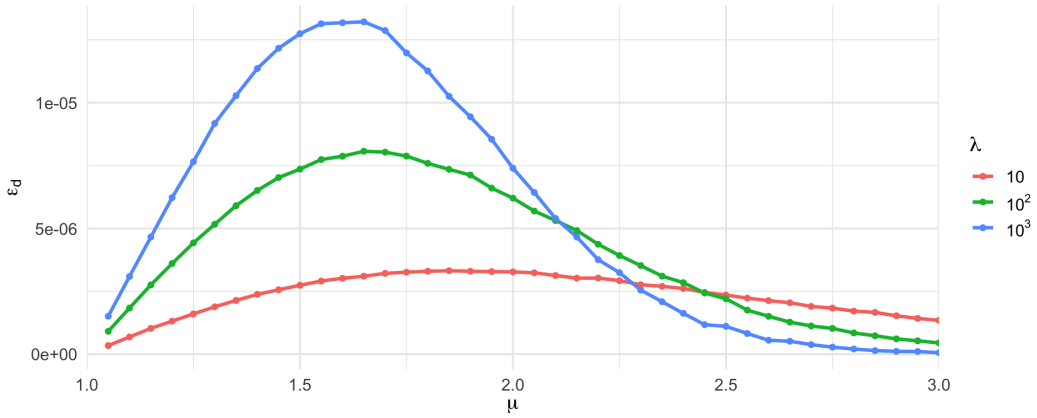

Figure 4.5: Relative error between η_{d1} and corrected η_{d2}^{corr}, showing near-equivalence when covariance is included.

4.3.2 Nondestructive Foraging in 1D Lévy Flights

We now turn to the nondestructive case. Figure 4.6 presents the estimator η_{nd2} as predicted by Eq. (3.10), alongside its approximation Eq. (3.11). Mirroring the destructive case, the approximation deviates from the exact expression near $\mu = 2$, with highest fidelity at the extremes $\mu \approx 1$ and $\mu \approx 3$. This reinforces the limitation of asymptotic approximations in intermediate regimes discussed in Section 3.2.

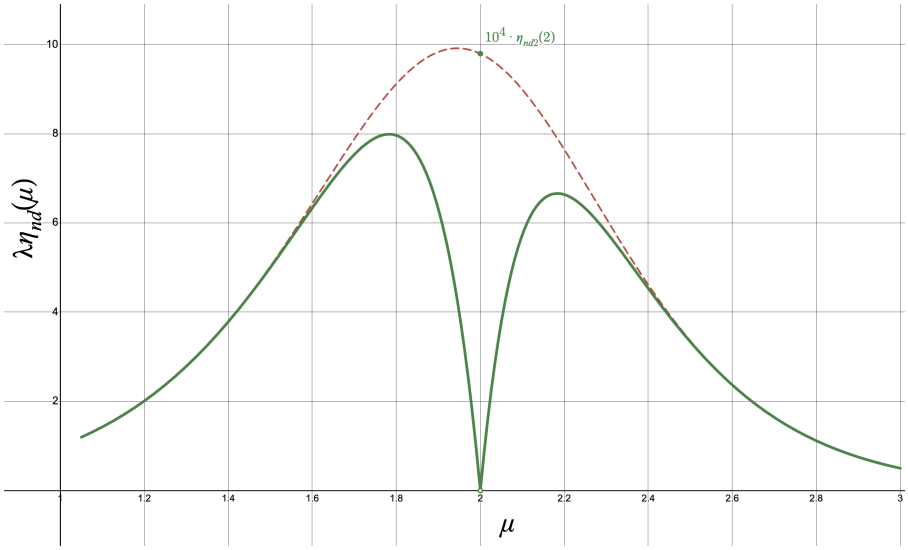

Figure 4.6: Theoretical estimator η_{nd2} for nondestructive foraging. The red dashed curve shows the exact expression for $\lambda = 10^4$, and the green curve shows the approximation. Parameters: $K = 1$, $r_v = 1$.

Simulation results for η_{nd1} and η_{nd2} (Fig. 4.7) reveal qualitatively similar trends across μ and λ, but with notable quantitative divergences. Crucially, discrepancies peak in the regime $\mu \in (2, 3)$ and amplify with λ, a distinct shift from the destructive case where maximal errors occurred at $\mu < 2$. For $\lambda = 10^4$, η_{nd1} remains below 15 while η_{nd2} exceeds 30, underscoring the severity of the mismatch in this region. Notably, a local maximum near $\mu = 2$ is also observed, consistent with findings reported in [6].

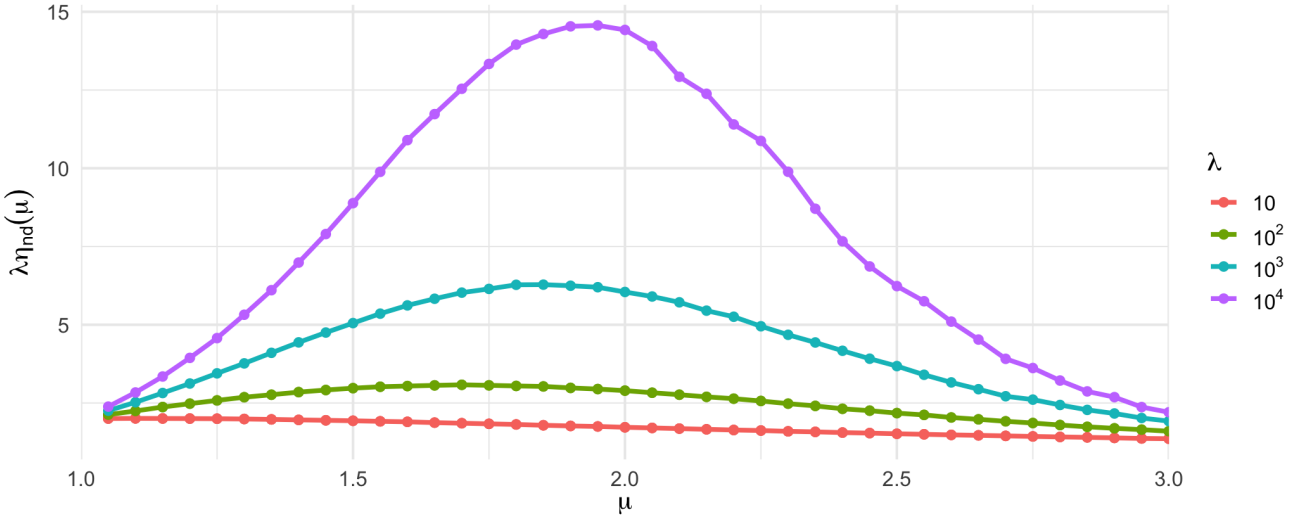

(a) Simulated estimator η_{nd1}

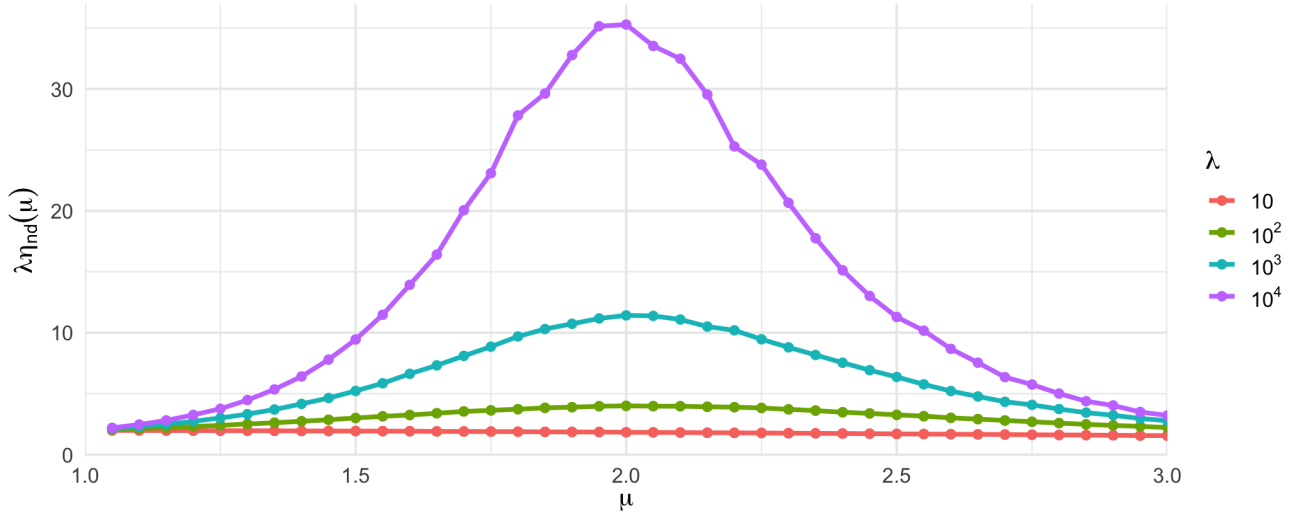

(b) Simulated estimator η_{nd2}

Figure 4.7: Simulated estimators η_{nd1} and η_{nd2} for nondestructive foraging. Discrepancies increase for moderate μ and large λ.

Quantifying this via relative error $\varepsilon_{nd} = |\eta_{nd1} - \eta_{nd2}|/\eta_{nd1}$ (Fig. 4.8) confirms maximal deviations in $\mu \in (2, 3)$. The error grows systematically with λ, reaching $\varepsilon_{nd} > 1$ for $\lambda = 10^4$ and $\mu \approx 2$.

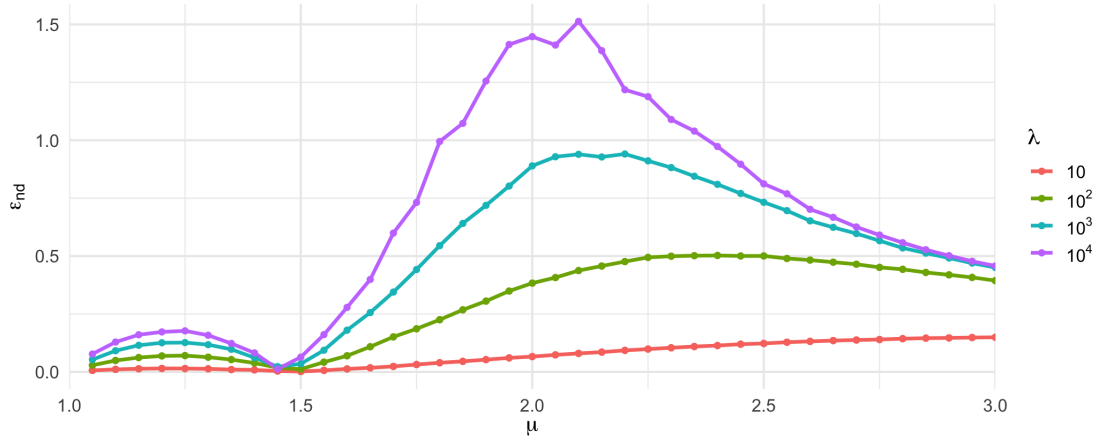

Figure 4.8: Relative error ε_{nd} between η_{nd1} and η_{nd2} across μ for various λ. The error increases for moderate μ and large λ.

The discrepancy arises because the assumption of independence between N_{nd} and $\bar{\ell}$ does not hold. Figure 4.9 shows that the correlation changes sign, being negative for $\mu < 1.5$, which means longer steps tend to reduce the number of steps taken, but becoming positive for $\mu > 2$, where longer steps actually increase the total steps. Although the correlation coefficient $\rho(N_{nd}, \bar{\ell})$ decreases with increasing λ, the covariance magnitude grows (see Fig. 4.10), indicating that the dependence between N_{nd} and $\bar{\ell}$ remains significant.

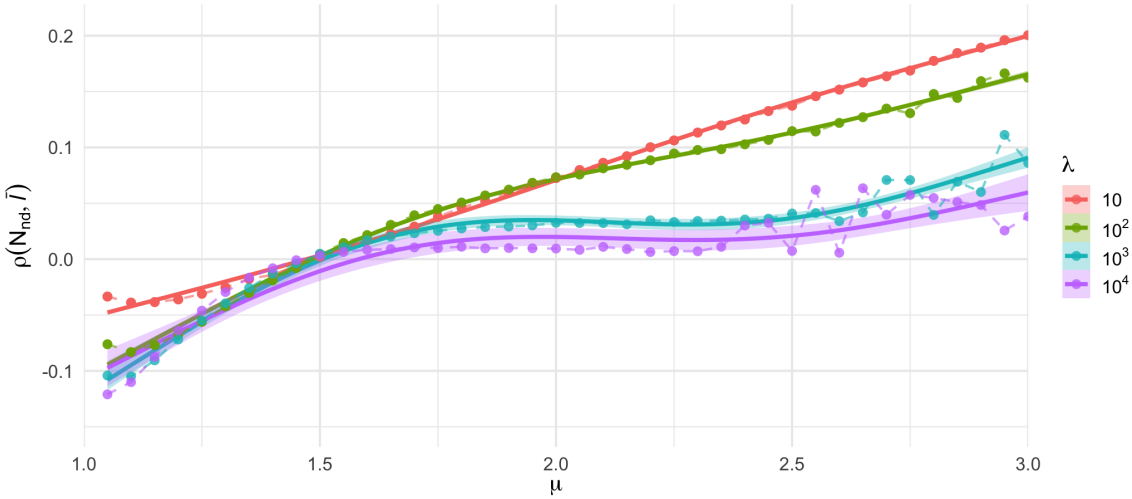

Figure 4.9: Pearson correlation coefficient $\rho(N_{nd}, \bar{\ell})$ between step count N_{nd} and mean step length $\bar{\ell}$ for nondestructive Lévy foraging, as a function of μ and λ. The smoothed curves (with 95% confidence bands) reveal a transition from negative correlation at low μ to positive correlation at high μ, with the transition occurring earlier for larger λ. While ρ weakens with increasing λ, the covariance $\mathrm{Cov}(N_{nd}, \bar{\ell})$ grows (see Fig. 4.10), indicating persistent dependence between N and $\bar{\ell}$ despite the smaller normalized correlation. This breakdown in independence explains discrepancies between efficiency metrics η_{nd1} and η_{nd2}.

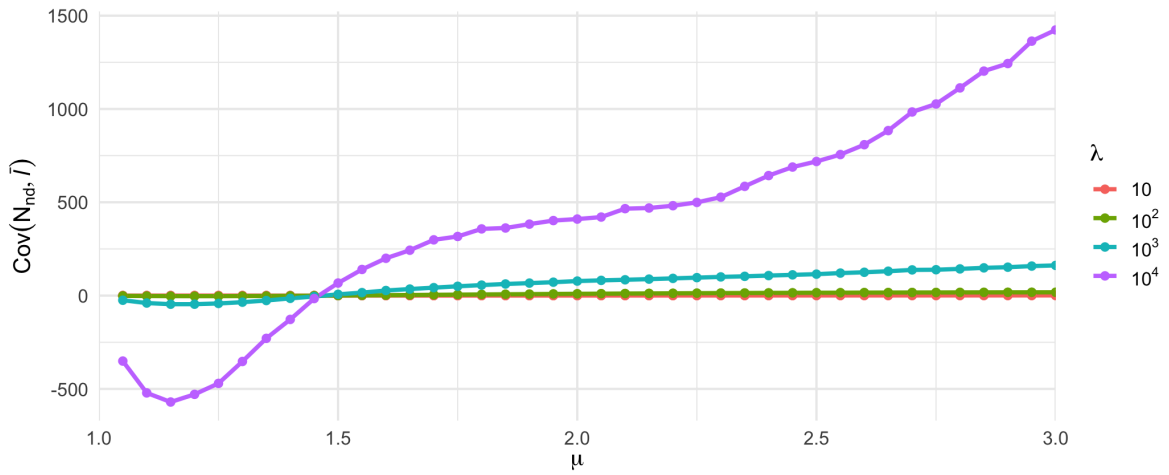

Figure 4.10: Covariance $\mathrm{Cov}(N_{nd}, \bar{\ell})$ for various λ. Despite weaker correlations at large λ, the covariance remains significant.

Incorporating the covariance via $\eta_{nd2}^{\mathrm{corr}} = [(\eta_{nd2})^{-1} + \mathrm{Cov}(N_{nd}, \bar{\ell})]^{-1}$ reduces relative errors to negligible levels (lower than 2×10^{-5} seen in Fig. 4.11). This confirms that covariance drives the estimator divergence.

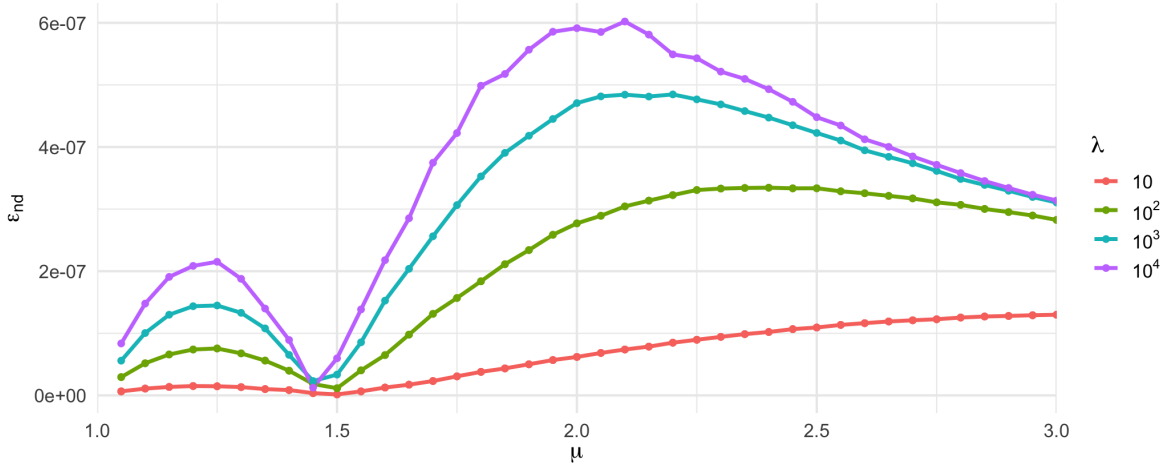

Figure 4.11: Relative error between η_1 and the corrected estimator $\eta_{nd2}^{\mathrm{corr}}$. The error drops to below $6 \cdot 10^{-7}$, confirming near-equivalence when covariance is included.

In the nondestructive case, the discrepancy between estimators reaches its maximum near $\mu = 2$. While correlations between steps weaken with increasing λ, the covariance remains significant and continues to cause differences between η_{nd1} and η_{nd2}. These results again emphasize the importance of clearly stating which efficiency estimator is being used, as they can differ quite a lot in this regime.

Chapter 5

Competition Dynamics in Two Dimensions

5.1 Clustering and Pattern Formation

Under certain conditions, competitive interactions between individuals can lead to clustering and the formation of regular spatial patterns [3]. This occurs when the effects of random movement are not strong enough to diffuse inhomogeneities and maintain an even distribution.

Throughout this chapter, we will assume that **environmental resources are uniformly distributed** in space. As a result, individual behavior is influenced mainly by how many other individuals are nearby, rather than by differences in resource availability across space. This simplifies the analysis and allows us to focus on how movement and competition alone can give rise to spatial structure.

In this context, competition causes individuals to aggregate, while random motion works to spread them out, opposing cluster formation.

In the following, we will explore two different models of competitive interactions[1], each with distinct parameters. By varying these interaction parameters, we will investigate how they influence the formation or absence of clusters and spatial patterns.

[1]By "competitive interactions", we refer to mechanisms where individuals influence each other's behavior such that the density of individuals in certain areas can increase or decrease.

5.2 Competing Bugs Model

To understand how patterns form, we consider a simple model of competing bugs. These bugs reproduce asexually and are represented as point-like particles. At time t, the system contains $N(t)$ individuals located at positions $x_i(t)$, where $i = 1, 2, \ldots, N(t)$. They move within a square domain of size $L \times L$.

Each bug's likelihood of reproducing or dying depends on the number of nearby neighbors. Since resources are assumed to be uniformly distributed in space, a bug's chances of feeding and reproducing depend only on local crowding, not on absolute position. We define an interaction radius R, and count the number of neighbors within this distance. Each individual's reproduction and death events are modeled as independent Poisson processes governed by

$$r_{\mathrm{b}}^{\mathrm{i}} = \max\left(0, r_{\mathrm{b}}^{0} - \alpha N_R^{\mathrm{i}}\right), \quad r_{\mathrm{d}}^{\mathrm{i}} = r_{\mathrm{d}}^{0} + \beta N_R^{\mathrm{i}} \tag{5.1}$$

Where:

- r_{b}^{i} and r_{d}^{i} are the individual birth and death rates for bug i.
- r_{b}^{0} and r_{d}^{0} are the baseline birth and death rates, respectively, when no neighbors are nearby.
- N_R^{i} is the number of neighbors within distance R from individual i.
- α and β are positive parameters controlling how neighbors affect reproduction and death.
- The $\max(0, \cdot)$ function ensures that reproduction cannot become negative.

This setup helps us understand how local interactions lead to clustering. In crowded areas, bugs reproduce less and die more due to intense competition, while in less crowded spots, they face weaker pressure. Now, if two clusters are close, separated by more than R but less than $2R$, the space between them is influenced by competition from both groups. This overlap creates the **death zone**, where the combined competitive pressure makes survival difficult. Figure 5.1 illustrates this mechanism.

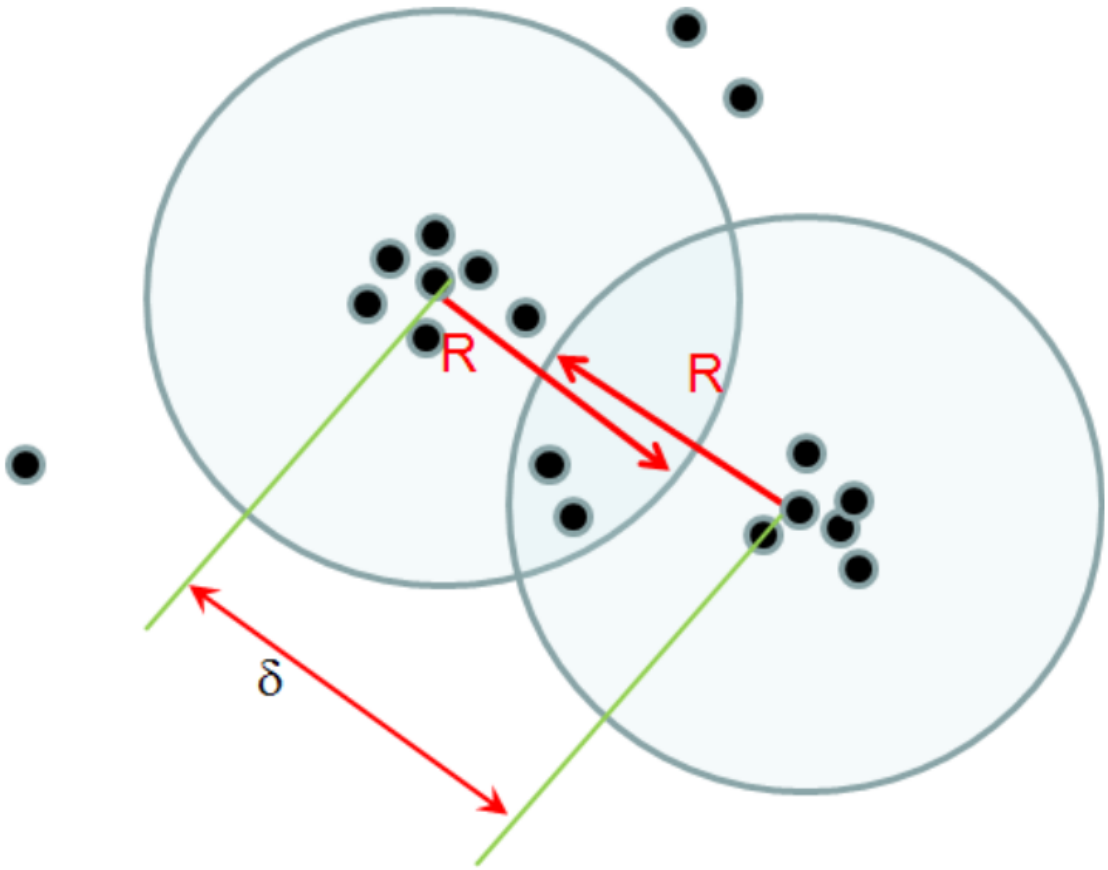

Figure 5.1: A sketch from [3] illustrating the clustering mechanism. Two clusters are separated by a distance δ between R and $2R$. The shaded circles represent the competition ranges. The overlapping region, the death zone, is subject to strong competition from both sides.

This creates a feedback loop. Dense regions remain populated, while the gaps between them tend to stay empty. Over time, this leads to the formation of a regular pattern of clusters.

Random movement works against this process, spreading individuals more uniformly and trying to fill the empty areas.

In the end, whether clusters form depends on the balance between two opposing effects:

- **Competition**, which favors the separation of individuals into distinct groups,
- **Random motion** (diffusion), which pushes the system toward a uniform distribution.

If movement is too strong, especially with long jumps, it can prevent clusters from stabilizing. But when motion is slow enough, competition dominates, and clear spatial patterns emerge.

5.2.1 Mean-field Estimate of Equilibrium Density in the Bugs Model

Before exploring spatial patterns in simulations, it helps to first analyze the system with a mean-field approximation. This assumes individuals are evenly distributed and experience the same environment, so we can drop the individual index i and focus on average quantities: the average density ρ_0, the average number of neighbors N_R within range R, and the average birth and death rates, r_b and r_d. In this simplified view, we estimate the equilibrium density by balancing average births and deaths.

If the system is uniform, the average density ρ_0 is constant everywhere. Since N_R counts neighbors within a circle of radius R, we relate it to density by:

$$\rho_0 = \frac{N_R}{\pi R^2} \tag{5.2}$$

Using the mean-field form of the rates from Equation 5.1 (assuming all individuals experience the same local density), equilibrium requires equal birth and death rates:

$$r_\mathrm{b} = r_\mathrm{d} \quad \Rightarrow \quad r_\mathrm{b}^0 - \alpha N_R = r_\mathrm{d}^0 + \beta N_R \quad \Rightarrow \quad N_R = \frac{r_\mathrm{b}^0 - r_\mathrm{d}^0}{\alpha + \beta} \tag{5.3}$$

Substituting into the density relation:

$$\rho_0 = \frac{r_\mathrm{b}^0 - r_\mathrm{d}^0}{(\alpha + \beta)\pi R^2} \tag{5.4}$$

This provides a baseline estimate for the population density where births and deaths balance. It indicates when the population tends to grow, shrink, or remain stable depending on parameters. However, it is only an approximation and may differ from simulation outcomes.

The mean-field model assumes individuals are evenly spread out, but in practice, the combination of random movement and local interactions often leads to uneven distributions. These effects can cause the actual population density to deviate from the mean-field estimate: random local extinctions (regions where bugs die out by chance) may lower the density, while clustering can also enhance reproduction in some areas, pushing the density higher. So, the mean-field prediction may serve as either an upper or lower bound depending on the system's behavior.

Despite its limitations, this approximation offers a useful starting point. It captures the basic dynamics and helps us understand when the population is likely to survive or decline, even if exact values differ once spatial distribution and stochasticity are considered.

5.2.2 Dynamical Stabilization Criterion for the Bugs Model

To determine when the system has reached a statistically stable state, we monitor the total population size N_t over time. The goal is to detect when the population ceases to drift and begins fluctuating around a characteristic value, denoted N_{eq}, indicating that the system has reached a steady-state regime.

Birth and death events are modeled as independent Poisson processes at the individual level. Therefore, for a population of size N_{eq}, the total number of births B and deaths D during a time step can be expressed as sums of individual Poisson variables:

$$B = \sum_{i=1}^{N_{\text{eq}}} B_i, \quad B_i \sim \text{Poisson}(r_b^i), \qquad D = \sum_{j=1}^{N_{\text{eq}}} D_j, \quad D_j \sim \text{Poisson}(r_d^j).$$

Since the sum of Poisson-distributed variables is also Poisson-distributed, we have:

$$B \sim \text{Poisson}\left(\sum_i r_b^i\right), \quad D \sim \text{Poisson}\left(\sum_j r_d^j\right).$$

When N_{eq} is large, we can approximate these distributions using the Central Limit Theorem:

$$B \sim \mathcal{N}(\mu_B, \sigma_B^2), \qquad D \sim \mathcal{N}(\mu_D, \sigma_D^2),$$

with means and variances:

$$\mu_B = \sum_i r_b^i, \quad \sigma_B^2 = \sum_i r_b^i, \qquad \mu_D = \sum_j r_d^j, \quad \sigma_D^2 = \sum_j r_d^j.$$

Defining the average birth and death rates as:

$$\overline{r_b} = \frac{1}{N_{\text{eq}}} \sum_i r_b^i, \qquad \overline{r_d} = \frac{1}{N_{\text{eq}}} \sum_j r_d^j,$$

we obtain:

$$\mu_B = \sigma_B^2 = N_{\text{eq}}\, \overline{r_b}, \qquad \mu_D = \sigma_D^2 = N_{\text{eq}}\, \overline{r_d}.$$

At equilibrium, we expect birth and death events to balance on average:

$$\overline{r_b} \approx \overline{r_d} \quad \Rightarrow \quad \mathbb{E}(B) \approx \mathbb{E}(D) \approx N_{\text{eq}} \cdot \overline{r_b}, \qquad \text{Var}(B) \approx \text{Var}(D) \approx N_{\text{eq}} \cdot \overline{r_b}.$$

To quantify how the population fluctuates around this balance, we look at the net population

change at each step ($\Delta t = 1$):

$$\Delta N = N_t - N_{t-1} = B - D.$$

Since B and D are independent and approximately normal, their difference is also normally distributed:

$$\mathbb{E}(\Delta N) = 0, \qquad \mathrm{Var}(\Delta N) = \mathrm{Var}(B) + \mathrm{Var}(D) \approx 2N_{\mathrm{eq}} \cdot \overline{r_b}.$$

Under a mean-field approximation, $\overline{r_b}$ is expected to converge to a steady value. While this may not hold exactly in all situations, our main goal here is to understand how fluctuations scale with respect to the equilibrium population size N_{eq}, which is a key variable we want to track explicitly. Therefore, we aim to eliminate other parameters in favor of expressing the dependence on N_{eq}.
Assuming

$$r_b = r_{\mathrm{b}}^0 - \alpha N_{\mathrm{R}} = \frac{\beta r_{\mathrm{b}}^0 + \alpha r_{\mathrm{d}}^0}{\alpha + \beta},$$

and fix $r_{\mathrm{b}}^0 = 1$, $r_{\mathrm{d}}^0 = 0.1$, while keeping $\alpha \ll \beta$, then $r_b \approx 1$ during equilibrium. Consequently, the fluctuation in population size becomes:

$$\Delta N \sim \mathcal{N}\left(0, 2N_{\mathrm{eq}}\right),$$

so the standard deviation of fluctuations grows like $\sqrt{2N_{\mathrm{eq}}}$, meaning it scales with the square root of the population size.

To avoid misinterpreting early transient noise as stabilization, we discard the first 45 steps of each simulation. After this warm-up period, we define a threshold:

$$\delta = c \cdot \sqrt{2N_{\mathrm{eq}}}, \quad \text{with } c = 1,$$

corresponding to one standard deviation. Since ΔN is approximately normal, about 68% of values should fall within $[-\delta, \delta]$:

$$P(|\Delta N| < \delta) \approx 0.6826.$$

To ensure robustness, we require this condition to hold for 15 consecutive steps. The probability of this happening by chance is:

$$(0.6826)^{15} \approx 0.01,$$

implying a 99% confidence that the system has reached a stable state.

In summary, we declare the system statistically stable when $|\Delta N| < \delta$ for 15 consecutive steps after a warm-up phase of 45 steps. During this stable period, we estimate N_{eq} using a moving time window. To handle cases where convergence is slow or not achieved, we impose a maximum cap of 150 steps. Figure 5.2 illustrates this process.

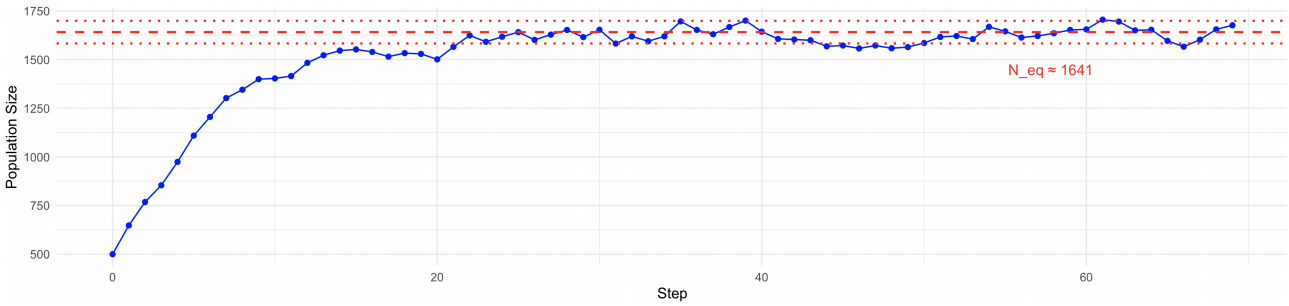

Figure 5.2: Population size evolution for $\mu = 2$, $R = 0.1$, $\alpha = 0$, $\beta = 0.02$. Stabilizes at step 69 with equilibrium $N_{\text{eq}} \approx 1641$. Red dashed line: equilibrium. Dotted lines: stability threshold.

5.2.3 Influence of Parameters on Clustering in the Bugs Model

We now investigate how different model parameters affect the emergence and structure of clusters. To isolate the influence of each, we perform simulations in which only one parameter is varied at a time. The parameters examined are the Lévy flight exponent μ, the interaction range R, and the competition coefficients α and β. All simulations are conducted with periodic boundary conditions: individuals exiting one side of the domain re-enter from the opposite side, forming a continuous space without borders.

To ensure reproducibility, all runs start from the same initial configuration, generated using a fixed random seed. This common starting state, shown in Figure 5.3, consists of 500 individuals with all having $r_{\text{d}}^0 = 0.1$ and $r_{\text{b}}^0 = 1$. For each set of parameters, we show the final configuration after the system reaches dynamical stability, as defined in the previous section. This approach allows a direct visual comparison of how each parameter influences clustering behavior.

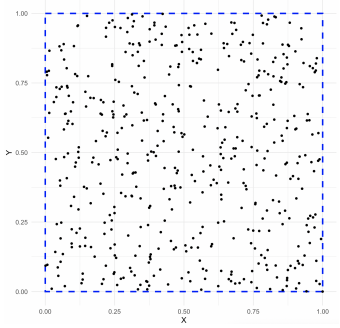

Figure 5.3: Initial configuration of the 500 walkers used in all simulations.

5.2.3.1 Varying the Lévy Flight Exponent μ

The exponent μ controls how often individuals make long jumps. Smaller values lead to more frequent long jumps, spreading individuals out and reducing clustering, while larger values produce more localized movement and promote aggregation.

Figure 5.4 shows clustering patterns for different μ values at fixed parameters $R = 0.01$, $\beta = 0.02$, and $\alpha = 0$. Each panel corresponds to a simulation snapshot after stability is reached, with the number of walkers indicated.

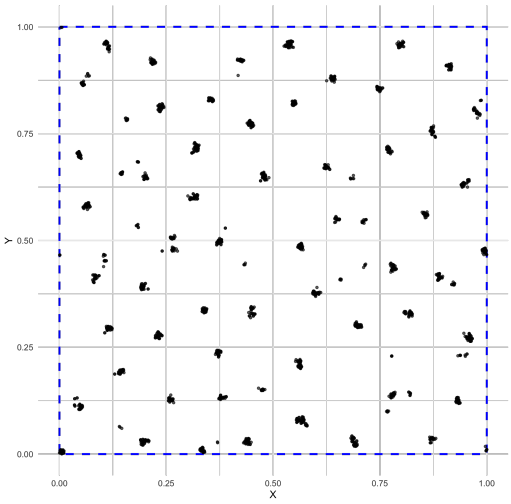

(a) $\mu = 10$, Step: 59, $n_{\text{walkers}} = 2429$

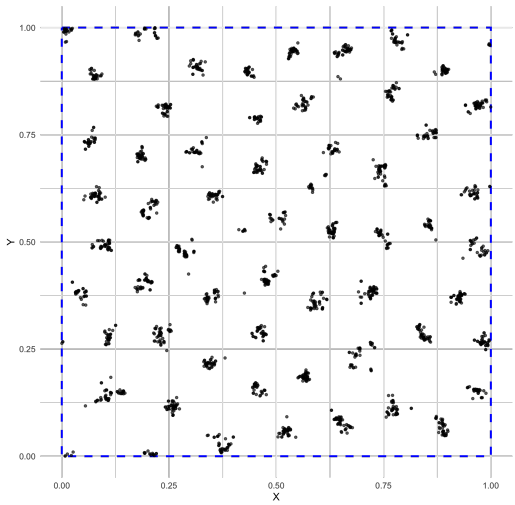

(b) $\mu = 3$, Step: 103, $n_{\text{walkers}} = 2265$

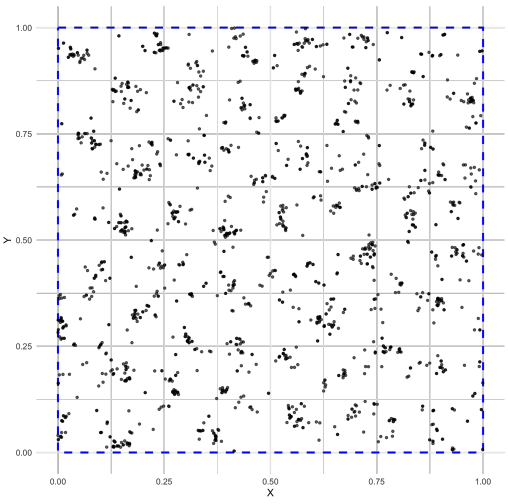

(c) $\mu = 2$, Step: 69, $n_{\text{walkers}} = 1676$

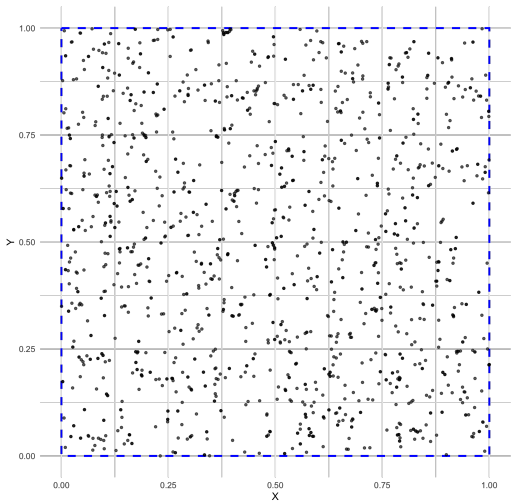

(d) $\mu = 1.5$, Step: 59, $n_{\text{walkers}} = 1393$

Figure 5.4: Clustering patterns for different Lévy flight exponents μ at fixed $R = 0.01$, $\beta = 0.02$, and $\alpha = 0$. Lower μ values lead to less distinct clusters, sometimes disappearing entirely. Image (a) shows Brownian-like behavior ($\mu > 3$).

Comparing panels (a) and (b) in Fig. 5.4, the number of particles is similar (around 2600), but spatial organization differs. Panel (b), with Lévy statistics, shows looser clusters and many isolated particles between them. The increased chance of long jumps causes particles to appear temporarily in gaps before moving on or dying. Panel (a) represents Brownian diffusion, producing denser clusters with less dispersion.

Panel (c) shows further weakening of cluster formation as long jumps become more frequent. In panel (d), clustering is suppressed, and the distribution remains roughly homogeneous, resembling the initial state. Here, long jumps dominate over competition, preventing aggregation.

5.2.3.2 Varying the Interaction Range R

The interaction range R sets how close individuals must be to interact. Larger R expands the scope of competition, promoting cluster formation. Smaller R limits interactions, which can slow or prevent clustering. When $R = 0$, individuals do not interact, so no clusters form.

Figure 5.5 illustrates how changing R affects clustering:

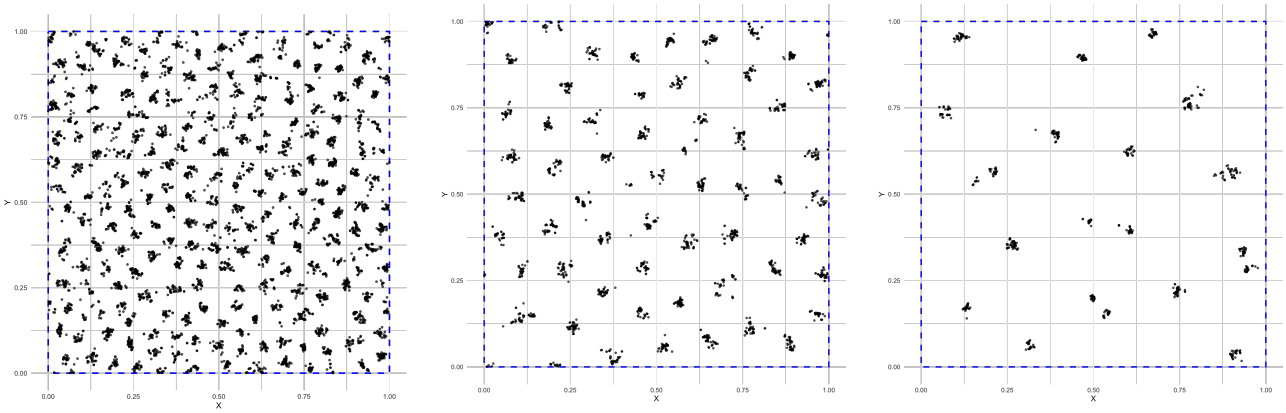

(a) $R = 0.05$ (b) $R = 0.1$ (c) $R = 0.2$

Figure 5.5: Effect of varying the interaction range R on clustering, with fixed $\mu = 3$, $\beta = 0.02$, and $\alpha = 0$. As R increases, longer-range interactions strengthen aggregation and create more defined patterns. Snapshots taken at: (a) Step 67, $n_{\text{walkers}} = 7492$; (b) Step 103, $n_{\text{walkers}} = 2265$; (c) Step 73, $n_{\text{walkers}} = 690$.

As R increases, clusters become more distinct and tend to organize into a regular, hexagonal-like pattern, showing that the interaction range affects cluster arrangement. Additionally, smaller R values allow more clusters to form closer together, resulting in a higher total number of walkers occupying the space compared to larger R, where clusters are fewer and more widely spaced.

5.2.3.3 Varying the Competition Parameter α

Next, we focus on the effect of the competition parameter α while keeping $\beta = 0$, isolating how competition impacts reproduction without affecting death rates. Increasing α makes reproduction become harder in denser areas.

Figure 5.6 compares final spatial configurations for $\alpha = 0.02$ and $\alpha = 0.04$, with all other parameters fixed. As expected, stronger competition leads to fewer individuals at steady state.

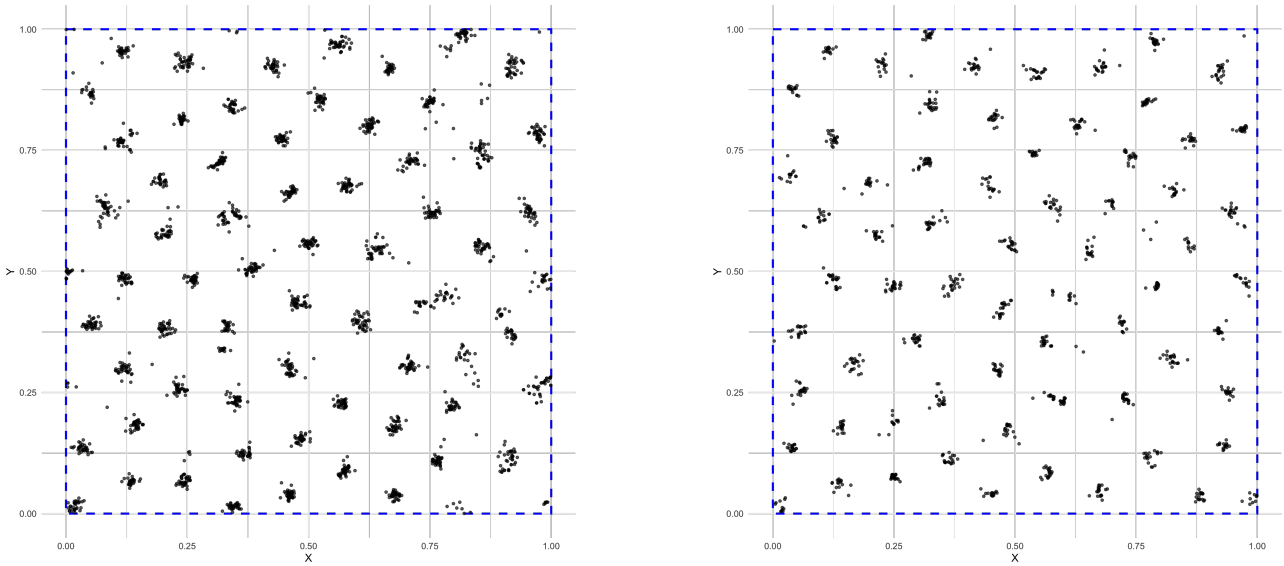

(a) $\alpha = 0.02$, Step: 62, $n_{\text{walkers}} = 2602$

(b) $\alpha = 0.04$, Step: 59, $n_{\text{walkers}} = 1327$

Figure 5.6: Effect of increasing α on clustering and population size, with fixed $\mu = 3$, $\beta = 0$, and $R = 0.1$. Higher α lowers population and weakens clustering.

While clustering patterns remain similar, the total population roughly halves when α doubles. This matches the mean-field prediction (equation 5.4), which shows an inverse relation between α and equilibrium population density. Stronger local competition reduces reproduction and thus limits how many individuals the environment can support.

5.2.3.4 Effect of μ on clustering with competition parameters $\alpha = \beta = 0.02$

Now we investigate the impact of varying the Lévy exponent μ on clustering patterns, with fixed competition parameters $\alpha = \beta = 0.02$. Specifically, we examine the cases where $\mu = 2$ and $\mu = 3$. As μ controls the probability of long jumps, we expect that increasing μ will influence the spread of the population. With the added competition, we anticipate that clustering will persist but with fewer individuals between the clusters, as stronger competition reduces reproduction in less crowded regions.

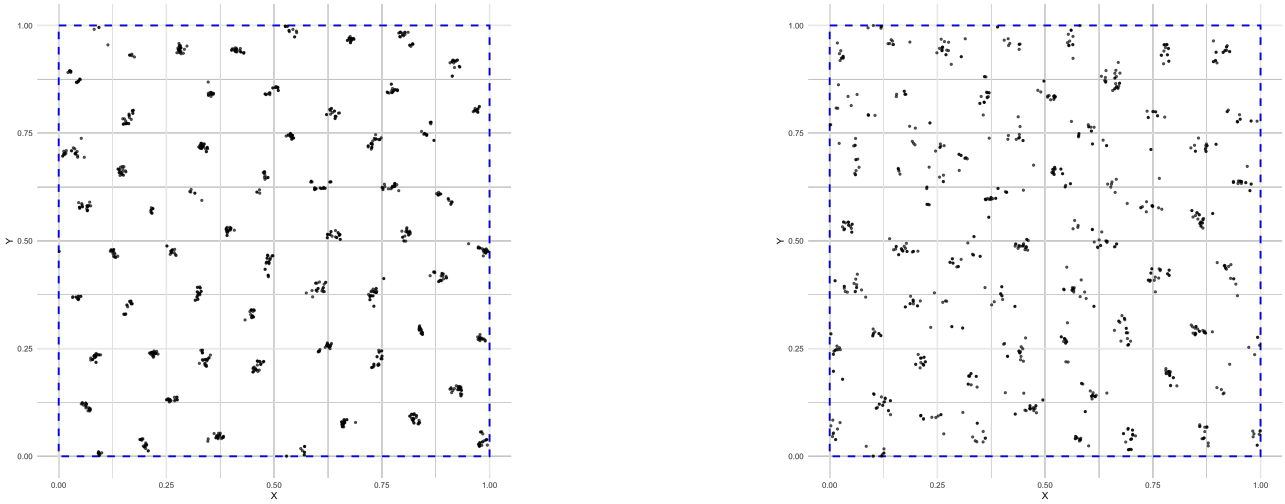

(a) $\mu = 3$, Step: 76, n_{walkers}: 1207

(b) $\mu = 2$, Step: 98, n_{walkers}: 933

Figure 5.7: Effect of changing the Lévy flight exponent μ on clustering when both competition and reproduction saturation are present ($\alpha = \beta = 0.02$). Parameters held constant: $\alpha = 0.02$, $\beta = 0.02$ and $R = 0.1$.

As shown in Figure 5.7, the clustering patterns for both $\mu = 2$ and $\mu = 3$ are similar to those in Figure 5.4 (where $\alpha = 0$). However, introducing competition ($\alpha = \beta = 0.02$) reduces the number of individuals both inside the clusters and in the spaces between them. This indicates that competition lowers population density in less crowded areas while strengthening cluster formation by encouraging individuals to group together. Although changing μ affects how widely the population spreads, competition sharpens the boundaries between clusters and helps keep each cluster compact and stable.

5.3 Motility Reduction Model

An alternative mechanism for cluster formation, distinct from reproduction and death-driven competition, is based on modulating the **motility** of individuals depending on their local environment. This idea draws inspiration from the concept of **Motility-Induced Phase Separation (MIPS)**, as described in the work of Cates and Tailleur [2].

Motility refers to the ability of an organism or particle to move through its environment. In biological or active matter systems[2], motility is often not constant. It can depend on factors such as crowding, chemical signals, or physical interactions. In the context of MIPS, motility

[2]Active matter is matter composed of large numbers of active "agents", each of which consumes energy in order to move or to exert mechanical forces [7].

decreases when local particle density increases, meaning that particles slow down in crowded regions.

In this model, instead of altering reproduction or death rates, particles all belong to the same species and interact purely through movement. Each particle slows down when it detects a higher number of neighbors within a certain radius. The idea is that densely packed regions reduce individual motility, making it harder for particles to escape. Over time, this feedback can lead to spontaneous aggregation, i.e, particles tend to accumulate where they are already dense, while sparse regions remain sparse.

We implement this mechanism using the same framework as in the bugs model but disable birth and death. Each particle performs a random step (e.g., a Lévy flight or Brownian motion), with the step length adjusted according to local crowding. Importantly, rather than reducing the speed as in classical MIPS, we reduce the jump length based on the number of neighbors within a radius R'. This distinction allows us to explore MIPS-like clustering through a different, yet related, route. Specifically, the movement step ℓ_i for individual i is defined as:

$$\ell_i = \ell_0 \cdot \exp(-\gamma N^i_{R'}) \tag{5.5}$$

where:

- ℓ_0 is the maximum step length in the absence of neighbors,
- $N^i_{R'}$ is the number of neighbors within radius R' around individual i,
- γ is a positive parameter controlling the strength of the slowdown effect.

To capture the gradual nature of this slowdown, each movement is executed over several substeps, during which the number of neighbors is recalculated. This allows the trajectory to adapt mid-step, resulting in stronger local feedback and a more realistic trapping mechanism in dense regions.

This model generates clusters not through survival dynamics, but via local self-trapping: particles effectively become "stuck" in regions where others are already present. Because the underlying mechanism differs from that of the competing bugs model, the resulting spatial patterns are also fundamentally distinct.

5.3.1 Dynamical Stabilization in the Motility Reduction Model

To determine when this self-trapping process leads to a steady state, we track the evolution of the *average adjusted step size* $\langle \ell \rangle$, that is, the actual jump length particles perform after their motility has been reduced by local interactions. We define equilibrium as the point when this motility becomes minimal and remains stable over some given time.

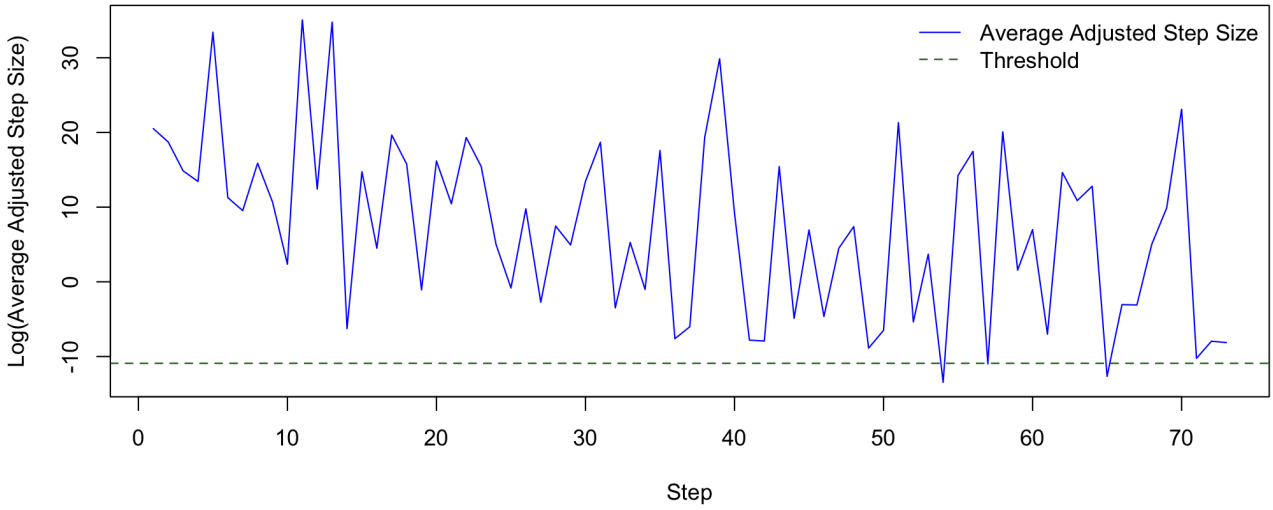

(a)

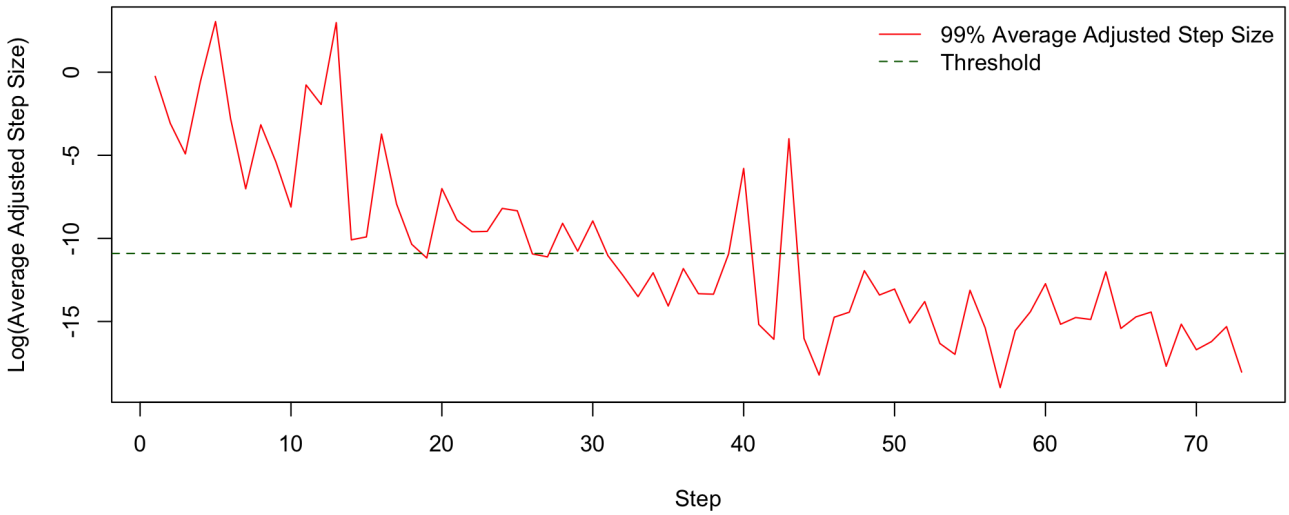

(b)

Figure 5.8: Time evolution of the average adjusted step size $\langle \ell \rangle$ in the motility reduction model with parameters $\mu = 1.2$, $R = 0.05$, $\gamma = 4$, and $\ell_{\min} = 0.001$. (a) shows the average over all walkers, while (b) excludes the top 1% of steps to mitigate the influence of rare, large jumps characteristic of Lévy flights.

Because Lévy flights naturally allow for rare but extremely long jumps, the global average step size can be heavily skewed by just a few particles. To avoid this, we compute the average over only 99% of the walkers, excluding the top 1% of largest steps at each time step. These outliers don't reflect the general behavior of the population and can mask the underlying trends. By removing them, we get a much clearer view of how the system as a whole is slowing down due to crowding, as shown in Figure 5.8.

To determine when the system has reached equilibrium, we compare this trimmed average to a theoretical threshold:

$$\ell_{\text{threshold}} = \ell_{\min} \cdot e^{-\gamma}$$

This threshold represents the expected step size of a particle that has exactly one neighbor and is moving with the minimal jump length. If the 99% average step size stays below this value for 30 consecutive main steps, we consider the system to be in a quasi-equilibrium. This 30-step window gives the system time to remain in a stable regime, while also keeping simulations computationally reasonable. The exact number isn't fixed, it can be tuned depending on the balance between precision and efficiency.

We can also interpret this threshold in a more intuitive way. It roughly corresponds to a situation where particles are moving in minimal pairs, with the smallest possible step size. Since pairs are the smallest meaningful group to consider clustering, this condition signals that the system has reached a state where clustering is sustained, and large-scale rearrangements are no longer taking place.

5.3.2 Influence of Parameters on Clustering in the Motility Reduction Model

In this section, we explore how different parameters in the model affect the clustering behavior of individuals. As before, we perform simulations where we vary one parameter at a time while keeping the others fixed, observing how these changes impact the emergence and structure of clusters. The parameters we explore include the Lévy flight exponent μ, the interaction range R', and the reduction factor γ. All simulations are run under periodic boundary conditions to avoid edge effects and starting with 500 walkers.

To ensure fair comparisons and reproducible results, we use the same initial seed across all runs. This means that the starting state is identical for every parameter combination,

as shown in Figure 5.9. First, we present this common initial configuration, followed by the final configuration captured once the system has reached a quasi-equilibrium state, defined previously. This allows us to observe how parameter changes influence both the speed and the pattern of clustering.

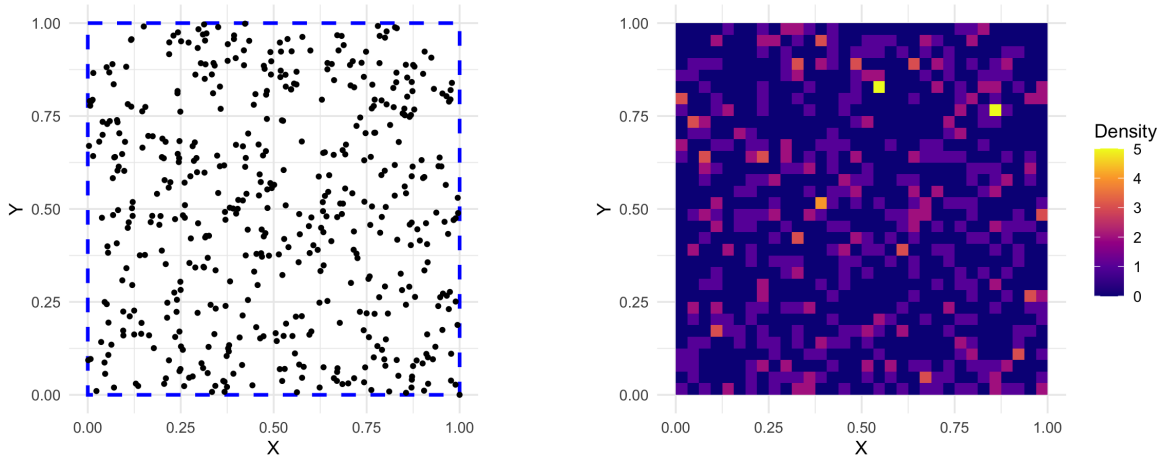

Figure 5.9: Initial configuration of the 500 walkers. On the left, the positions of the individual particles are shown, while on the right, a local density plot is presented. The space is divided into 32×32 squares, with the color intensity representing the number of particles within each square.

Alongside the scatter plots of individual positions, we also show local density maps. These provide an overview of how particles distribute across space by dividing the area into 32×32 cells and counting the number of individuals in each. Brighter regions correspond to higher local densities, highlighting emerging clusters, while darker areas indicate sparsity or emptiness.

5.3.2.1 Varying the Lévy Flight Exponent μ

To study the role of the Lévy exponent μ, we run simulations for several values while keeping the interaction range $R' = 0.05$ and the slowdown factor $\gamma = 4$ fixed. Below, each row shows a snapshot of the system, particle positions and density map, taken at the moment when the system reached quasi-equilibrium.

As shown in Figure 5.10, the Lévy exponent μ significantly influences how particles explore space and cluster. For $\mu = 2$, particle displacement is moderate and the configuration remains fairly uniform. When $\mu = 1.5$, movement becomes more heterogeneous, with slight inhomogeneities appearing. At $\mu = 1.2$, particles move more actively and begin to form well-defined, spatially localized clusters.

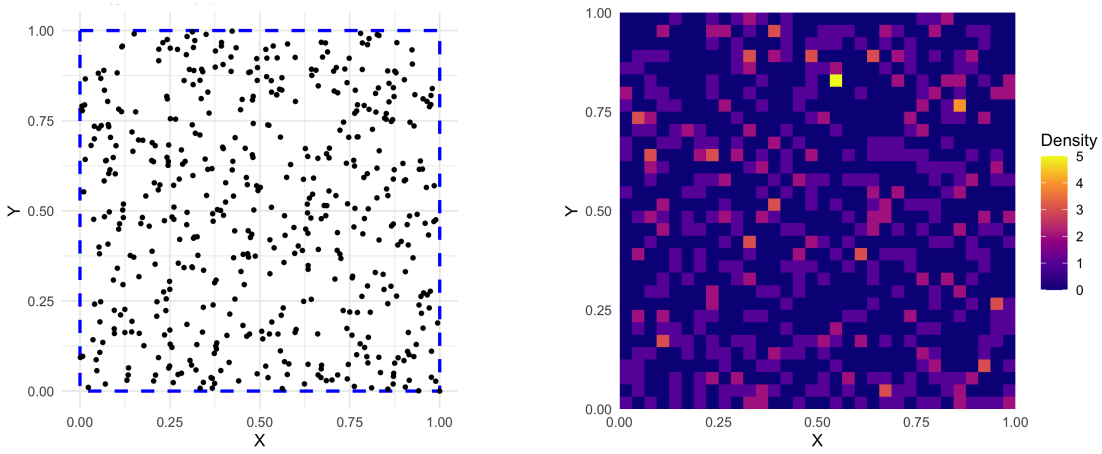

(a) $\mu = 2$, Step: 31

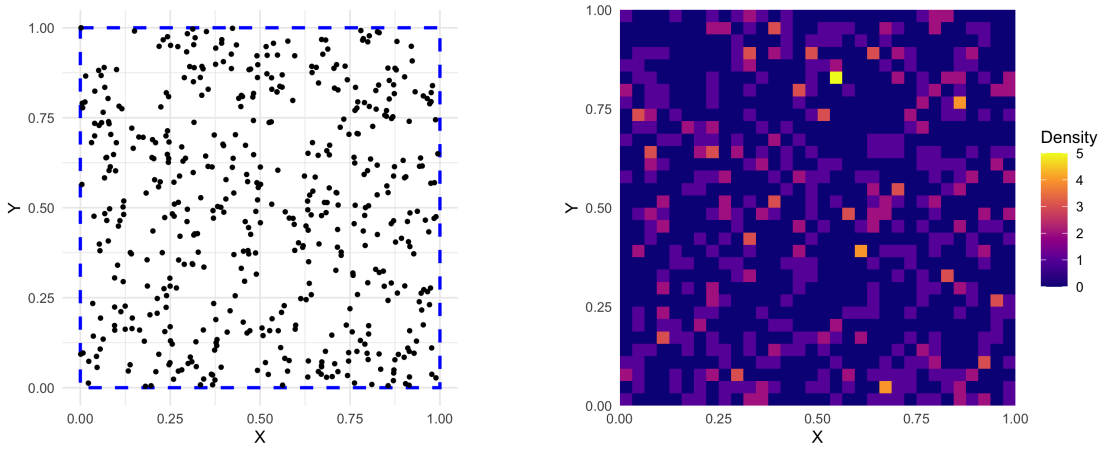

(b) $\mu = 1.5$, Step: 63

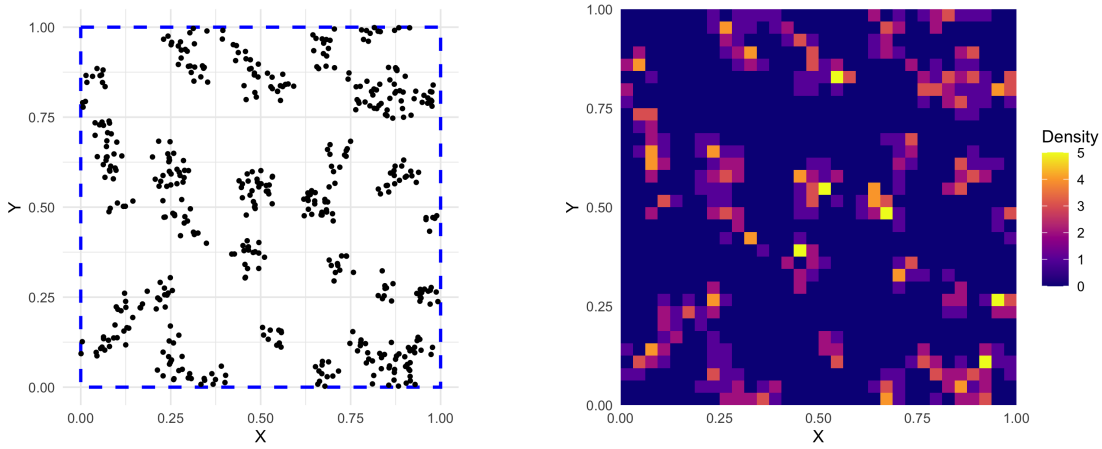

(c) $\mu = 1.2$, Step: 73

Figure 5.10: Effect of varying the Lévy exponent μ on the clustering dynamics in the motility reduction model. All simulations use interaction radius $R' = 0.05$ and slowdown factor $\gamma = 4$. As μ decreases from (a) to (c), clustering becomes more pronounced due to the higher frequency of short steps. Snapshots are taken at the moment each system reaches quasi-equilibrium, determined dynamically based on the stability of the average adjusted step size.

This trend aligns with the core mechanism of the model: clustering is driven by motion. Lower values of μ result in more frequent long steps, which enable faster exploration and more efficient aggregation. Since $\mu = 1.2$ leads to clearer clustering within a reasonable timescale, we use it as the default value in the subsequent parameter explorations.

5.3.2.2 Varying the Interaction Radius R'

Next, we explore how the interaction radius R' influences clustering behavior. The parameter R' determines the spatial extent over which particles perceive and respond to their neighbors, directly affecting how local crowding reduces movement. As such, it plays a central role in shaping the size, compactness, and speed of formation of the resulting clusters.

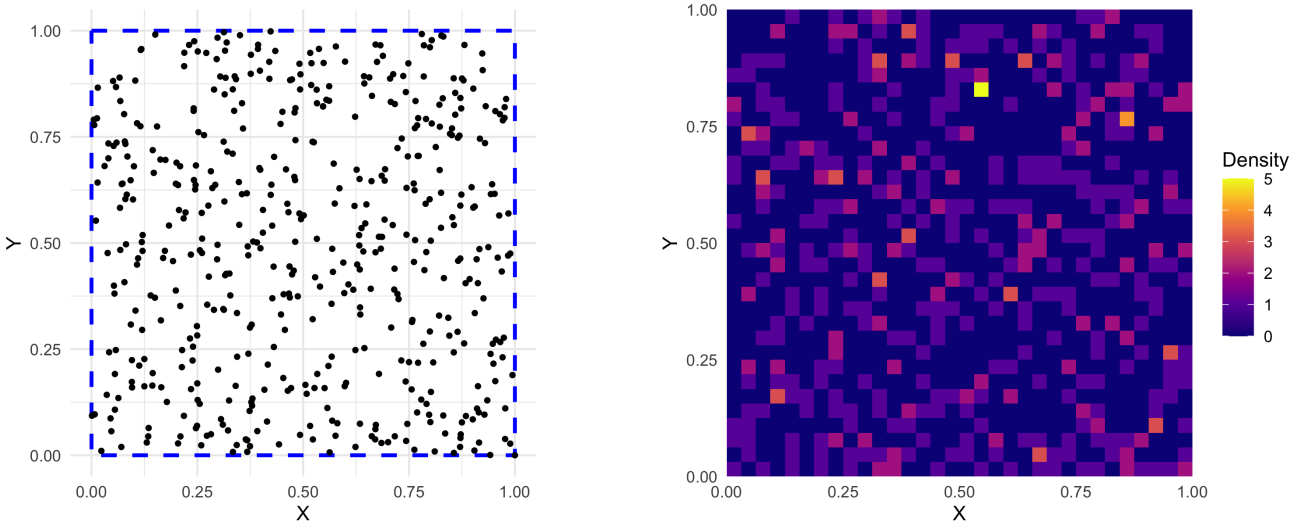

(a) $R' = 0.1$, Step: 30

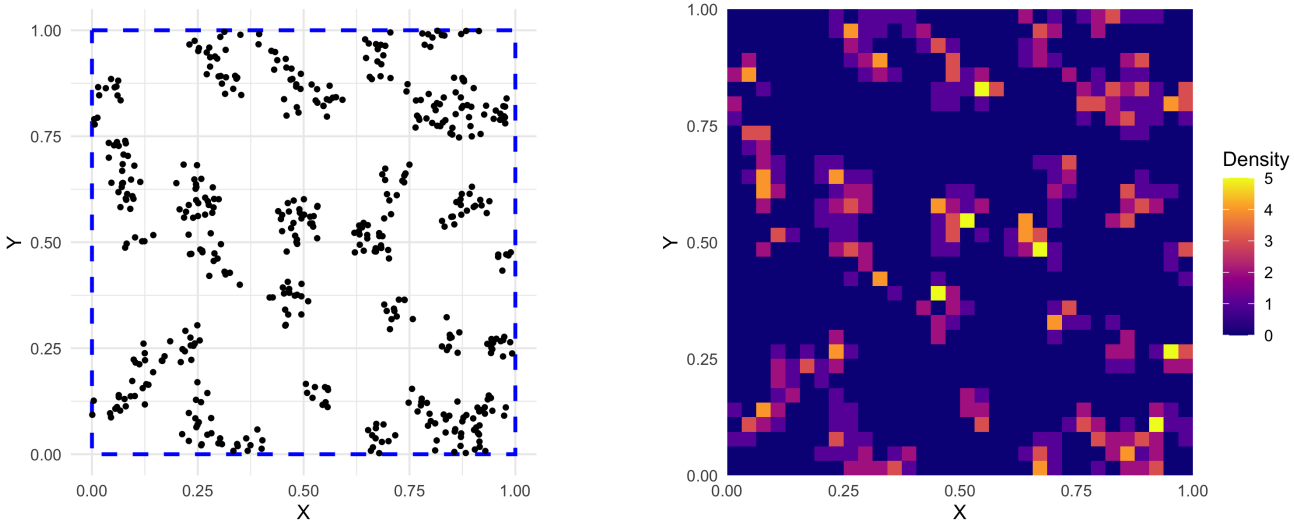

(b) $R' = 0.05$, Step: 73

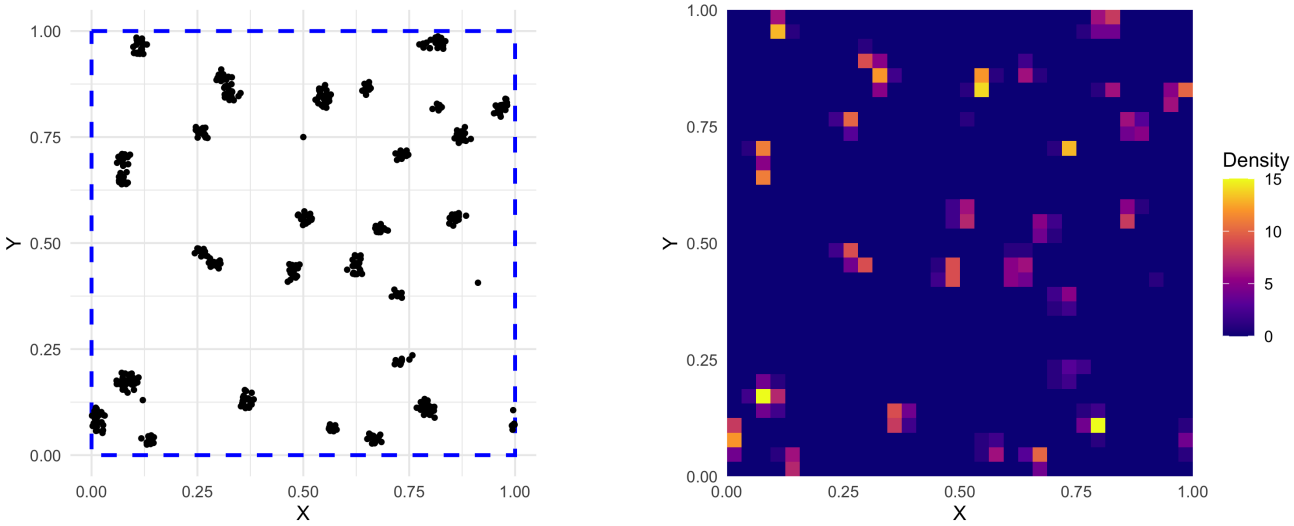

(c) $R' = 0.02$, Step: 102

Figure 5.11: Effect of varying the interaction radius R' on the clustering dynamics in the motility reduction model. All simulations use $\mu = 1.2$ and $\gamma = 4$, and snapshots are taken at the point where the system reaches quasi-equilibrium. As R' decreases from (a) to (c), clusters become increasingly compact and spatially localized. Smaller values of R' lead to stronger local interactions, which more rapidly inhibit movement and generate tightly bound aggregates.

As shown in Figure 5.11, when the interaction radius is large, like $R = 0.1$ in panel (a), each particle senses a lot of others around it. This strong interaction makes them slow down quickly, so the system stops changing early on. But because particles are already so restricted, they do not have much room to rearrange themselves. The result is a fairly even, unstructured distribution without clear clusters.

With a medium-sized radius, $R' = 0.05$ in panel (b), the interaction range is smaller. Particles can still move around a bit before getting stuck, which gives them time to gather into distinct groups. This leads to the formation of larger, well-spread clusters that are clearly visible and more organized.

Finally, when the radius is small, $R' = 0.02$ in panel (c), particles only slow down if they are really close to others. This means they move freely for longer, but once they find a dense spot, they quickly get stuck. The result is the formation of very tight, compact clusters that are strongly separated from each other.

In short, the interaction radius controls how tightly particles group together. Larger radii stop movement too early, preventing strong clustering. Smaller radii allow sharper, more compact clusters to form, but they take a bit longer.

5.3.2.3 Varying the Motility Reduction Parameter γ

The parameter γ controls how strongly a particle's movement is reduced when others are nearby. Higher values of γ mean stronger slowing down in crowded areas, making it harder for particles to explore space and form clusters. To understand the effect of γ, we revisit the case where clustering was previously absent: $R' = 0.1$, $\mu = 1.2$, and $\gamma = 4$ (see Figure 5.11(a)).

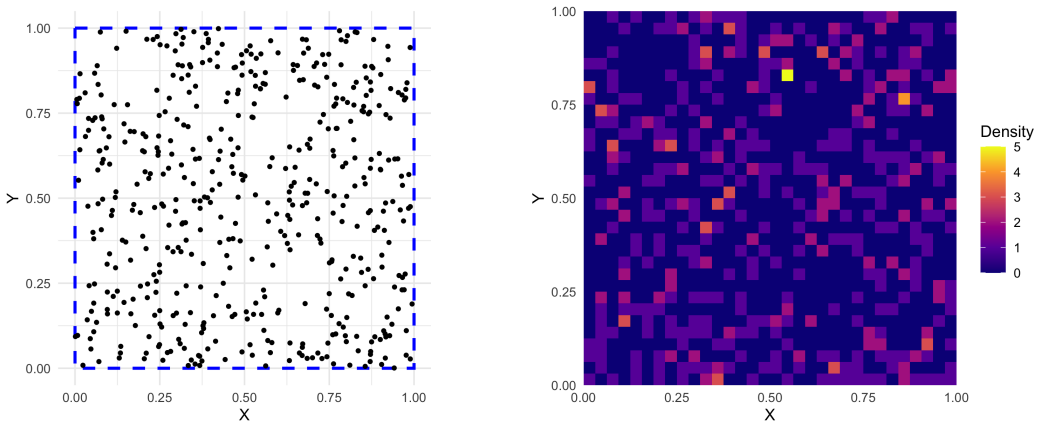

(a) $\gamma = 2$, Step: 30

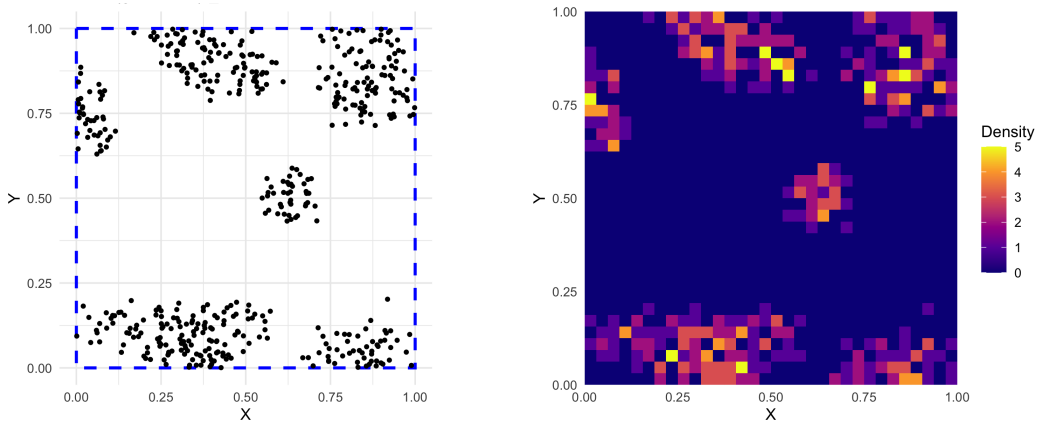

(b) $\gamma = 1$, Step: 108

Figure 5.12: Effect of reducing the motility inhibition factor γ on clustering dynamics. Here $R' = 0.1$ and $\mu = 1.2$ are fixed.

As shown in Figure 5.12, lowering γ makes a clear difference. When $\gamma = 2$ (panel (a)), clusters begin to form, although more slowly and less distinctly. Reducing γ further to 1 (panel (b)) leads to well-defined clusters, showing that particles can now move enough to find and stick to denser regions.

In summary, γ regulates how easily particles get "stuck" near others. When γ is too high, motion is suppressed too early, preventing clusters from forming. Lower values of γ keep particles mobile longer, allowing them to self-organize into distinct clusters. This highlights the importance of balancing movement and interaction strength to control clustering behavior.

5.4 Modeling Competition Between Different Species

We now explore how two distinct species compete for survival while freely moving in a space with uniformly distributed resources. Our approach builds on the bug and motility reduction models introduced earlier in this chapter, extending them to include inter-species competition mechanisms.

An individual's chances of reproducing or dying depend not only on the number of nearby individuals of the same species ("friends") but also on the number of individuals from the other species ("unfriends"). For any given individual, we will denote variables without hats as referring to its own species, and variables with hats as referring to the other species.

5.4.1 Competition Through Birth and Death Rates

In this model, birth and death rates are adjusted to capture competition both within and between species, defined as:

$$r_{\mathrm{b}}^{i} = \max\left(0, r_{\mathrm{b}}^{0} - \alpha N_R^i - \kappa_b \hat{N}_R^i\right), \quad r_{\mathrm{d}}^{i} = r_{\mathrm{d}}^{0} + \beta N_R^i + \kappa_d \hat{N}_R^i \tag{5.6}$$

where:

- N_R^i and $\hat{N}_R^i$ count friends and unfriends within radius R of individual i,
- κ_b and κ_d measure how competition from unfriends affects reproduction and death,
- r_{b}^{0}, r_{d}^{0}, α, and β are baseline parameters shared between species, controlling dynamics within friends.

Using a mean-field analysis (see Annex A.4), we find that local densities tend to balance dynamically, with $\hat{N}_R$ roughly equal to N_R, indicating potential coexistence.

As before, we consider the system stable when the total population fluctuates below a defined threshold, now evaluated over the combined population of both species. Specifically, stability is determined using N_{eq}, the mean total number of individuals over a moving window of 15 time steps. Although we now vary several interaction parameters, we retain the same stopping criterion used previously, based on the fluctuation scale $\sqrt{2N_{\mathrm{eq}}}$.

Additionally, to improve computational efficiency, simulations are stopped early if one species goes extinct, as further dynamics no longer reflect competitive interactions between both species. This approach ensures that the analysis focuses on meaningful coexistence or exclusion outcomes.

For simplicity, we assume both species share identical base birth and death rates, as well as the same α, β, κ_b and κ_d parameters governing interactions. These assumptions may be relaxed in future studies to investigate more complex scenarios.

5.4.2 Competition via Motility Effects

Next, we incorporate motility effects where a high local density of friends slows down movement, while nearby unfriends increase jump length.

Accordingly, the movement step ℓ_i for individual i is given by:

$$\ell_i = \ell_0 \cdot \exp(-\gamma_{\text{slow}} N^i_{R'} + \gamma_{\text{fast}} \hat{N}^i_{R'}) \tag{5.7}$$

where:

- ℓ_0 is the maximum step length without neighbors,
- $N^i_{R'}$ counts friends within radius R' around individual i,
- γ_{slow} controls how strongly friends slow down movement,
- γ_{fast} controls how much unfriends boost jump length.

Here, γ_{slow} models the motility reduction caused by crowding with friends, while γ_{fast} captures avoidance by increasing step size in the presence of unfriends. Note that R' is the interaction radius for motility, which may differ from R of the bugs model.

Finally, we continue to apply the same equilibrium condition as before. The system is considered stable when movement steps remain below the previously defined threshold.

5.4.3 Combining Birth-Death Competition and Motility Effects

Here we bring together the two ways species interact, by changing birth and death rates and by modifying their movement steps. This lets us study how competition through these interactions and motility-driven clustering work together to affect the dynamics between species. To keep the population size under control and speed up computations, we set the base birth rate to $r_{\mathrm{b}}^0 = 0.5$ and start with 250 walkers of each species spread uniformly across the space. Since we assume food or resources are evenly distributed, any patterns we see mostly come from how the species move and interact, not from resource differences.

We leave the other variables as $r_{\mathrm{d}}^0 = 0.1$, $\beta = 0.02$, $\alpha = 0$, $\kappa_d = \kappa_b = 0.03$, $R = 0.1$, $R' = R/2$, $\gamma_{\mathrm{fast}} = 0.04$, and $\gamma_{\mathrm{slow}} = 10 \cdot \gamma_{\mathrm{fast}}$. It is important to notice that in this case, being close to friends is the best way for a population to survive and grow. This is because competition interactions between species are stronger than within species, i.e. $\kappa_b > \alpha$ and $\kappa_d > \beta$. As a result, any individual near members of the other species faces a big handicap. Therefore, we expect some form of spatial separation that reduces direct competition between species.

We call one species A and the other B. We assign them different movement parameters μ so their movement patterns differ and they act as distinct species. We look at competition between Lévy and Brownian movers, as well as Lévy versus Lévy. For each setup, we compare runs with and without motility effects to see how changes in movement affect the outcome.

In all cases, we track both stopping conditions, the one based on birth and death fluctuations and the one based on movement steps. We stop the simulation when either condition is met.

Before analyzing the results, we clarify the notation used for local neighborhood densities, which are key to determining birth and death rates. For any individual i, we define:

$$N_R^{A,i} \quad \text{and} \quad N_R^{B,i}$$

as the number of same-species neighbors (type A or B, respectively) within a radius R, and:

$$\hat{N}_R^{A,i} \quad \text{and} \quad \hat{N}_R^{B,i}$$

as the number of neighbors of the *other* species within the same radius. For example, $\hat{N}_R^{A,i}$ gives the number of species B individuals near individual i of species A, while $\hat{N}_R^{B,i}$ counts species A neighbors around an individual of species B. These quantities determine the level of competitive pressure experienced by each walker during birth and death events due to neighbors.

5.4.3.1 Lévy vs. Brownian Walkers: Results and Observations

We explore how motility effects influences competition between species with different movement strategies. In both scenarios, species A performs Brownian motion ($\mu_A = 5$), while species B exhibits Lévy-like movement, first with $\mu_B = 2$, and later more strongly with $\mu_B = 1.5$. Figures 5.13 and 5.14 summarize the resulting dynamics under these conditions.

Without motility effects, Lévy walkers begin to surpass Brownian walkers by leveraging their ability to reach and occupy empty sites more quickly. This spatial advantage results in a population imbalance, eventually leading to competitive exclusion (Figure 5.13b).

Motility decreases near same-species neighbors, encouraging clustering, and increases when other species are nearby, causing avoidance between them. These mechanisms result in spatial patterns that reduce direct encounters between species and promote coexistence (Figure 5.13a), leading to a larger total population under the given parameters.

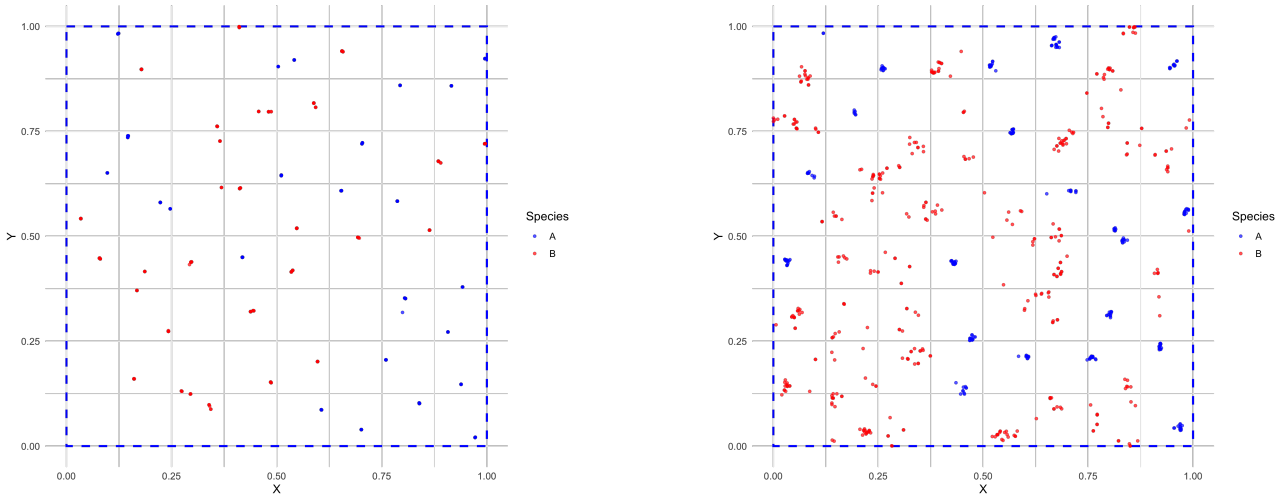

(a) Step: 59, $N_A = 432$, $N_B = 440$

(b) Step: 77, $N_A = 273$, $N_B = 433$

Figure 5.13: Competition between Brownian ($\mu_A = 5$) and Lévy ($\mu_B = 2$) walkers. (a) With motility effects, the two species coexist by forming separate spatial clusters that reduce direct competition. (b) Without motility effects, the Lévy walker (species B) outcompetes the Brownian walker (species A) by step 77, reaching nearly twice its population.

A more extreme case is shown in Figure 5.14, where species B has $\mu_B = 1.5$. In the presence of motility effects, coexistence is still achieved, though with more asymmetric population sizes. In contrast, removing this mechanism results in the complete extinction of species A by step 73.

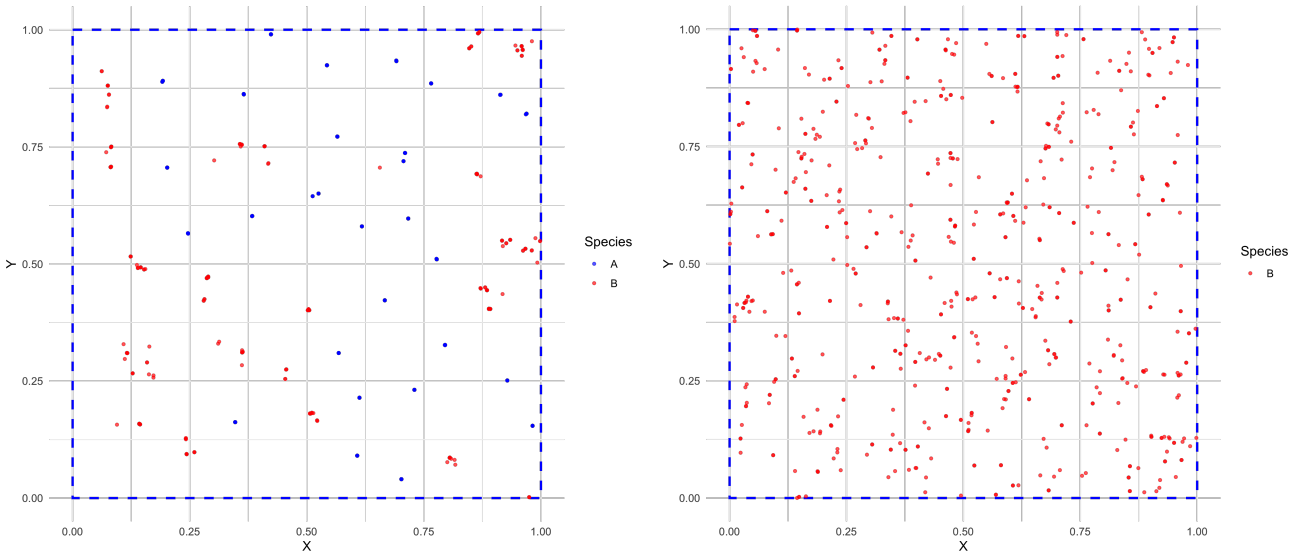

(a) Step: 59, $N_A = 482$, $N_B = 299$

(b) Step: 73, $N_A = 0$, $N_B = 637$

Figure 5.14: Competition between Brownian ($\mu_A = 5$) and Lévy ($\mu_B = 1.5$) walkers. (a) With motility effects, the two species coexist by forming separate spatial clusters, even when the Lévy walker is more exploratory (lower μ_B). (b) Without this effect, species B quickly dominates, and species A goes extinct by step 73. The enhanced exploratory power of the Lévy walker leads to faster competitive exclusion.

To understand why this happens, we must consider the initial conditions of the simulation. At $t = 0$, both species begin with 250 individuals uniformly distributed across space. Given this symmetry and the random placement of individuals, we can reasonably assume that the statistical properties of their local environments are equivalent. As a result, both species initially experience comparable birth and death rates, since the local densities N_R^i and $\hat{N}_R^i$ determining these rates are roughly the same for both species.

Now imagine what occurs just a few steps in. Some individuals die, creating random empty spots in the environment. Here is where the key asymmetry emerges: Lévy walkers, thanks to their longer jumps, are much more likely to reach and colonize these vacant sites. In contrast, Brownian walkers, taking only small steps, have a low probability of arriving at such gaps quickly.

As a result, newly opened spaces tend to be colonized by other Lévy walkers, meaning they end up more often surrounded by their own kind rather than by Brownian individuals, who are less likely to reach those sites.

This colonization difference leads to divergent neighborhood compositions:

$$\hat{N}_R^{B,i} \approx 0 \quad \text{(Lévy surrounded by friends)} \tag{5.8}$$

$$\hat{N}_R^{A,i} \gg 0 \quad \text{(Brownian surrounded by Lévy invaders)} \tag{5.9}$$

The competition hierarchy ($\kappa_b = 0.03 > \alpha = 0$, $\kappa_d = 0.03 > \beta = 0.02$) then amplifies this imbalance:

$$r_b^{A,i} = \max\left(0, 0.5 - \alpha N_R^{A,i} - \kappa_b \hat{N}_R^{A,i}\right) \to 0$$
$$r_d^{A,i} = 0.1 + \beta N_R^{A,i} + \kappa_d \hat{N}_R^{A,i} \gg 0.1$$

In this setup, Brownian walkers face a dead-end: they cannot escape, cannot reproduce effectively (low $r_b^0 = 0.5$ and high interspecies penalties), and slowly collapse under the weight of their surroundings. Clustering, which might otherwise offer protection, becomes a trap. On the other hand, Lévy walkers perform better by continuously colonizing space, keeping their densities moderate and their competition with the other species low.

Therefore, Lévy walkers maintain near-optimal rates:

$$r_b^{B,i} \approx 0.5$$
$$r_d^{B,i} \approx 0.1 + \beta N_R^{B,i}$$

This explains the rapid extinction observed in Figure 5.14b. Only motility effects prevent this cascade by promoting spatial segregation through self-trapping and reducing interspecies competition through avoidance.

To further explore this mechanism, we now consider the same scenario with $\mu_A = 5$ and $\mu_B = 1.5$, but increase the baseline birth rate to $r_\mathrm{b}^0 = 2$. This change reduces the penalty of crowding and allows clustered individuals, such as Brownian walkers, to sustain reproduction despite their limited motility. If our intuition is on the right track, this adjustment could allow the Brownian population to persist even without motility effects, as clustering becomes less detrimental and competition from Lévy walkers less overwhelming.

For this experiment, we deliberately extended the simulation to 200 steps, beyond the usual stopping point, to fully observe the long-term coexistence dynamics. Without this extension, the program would have terminated earlier, missing these steady-state behaviors.

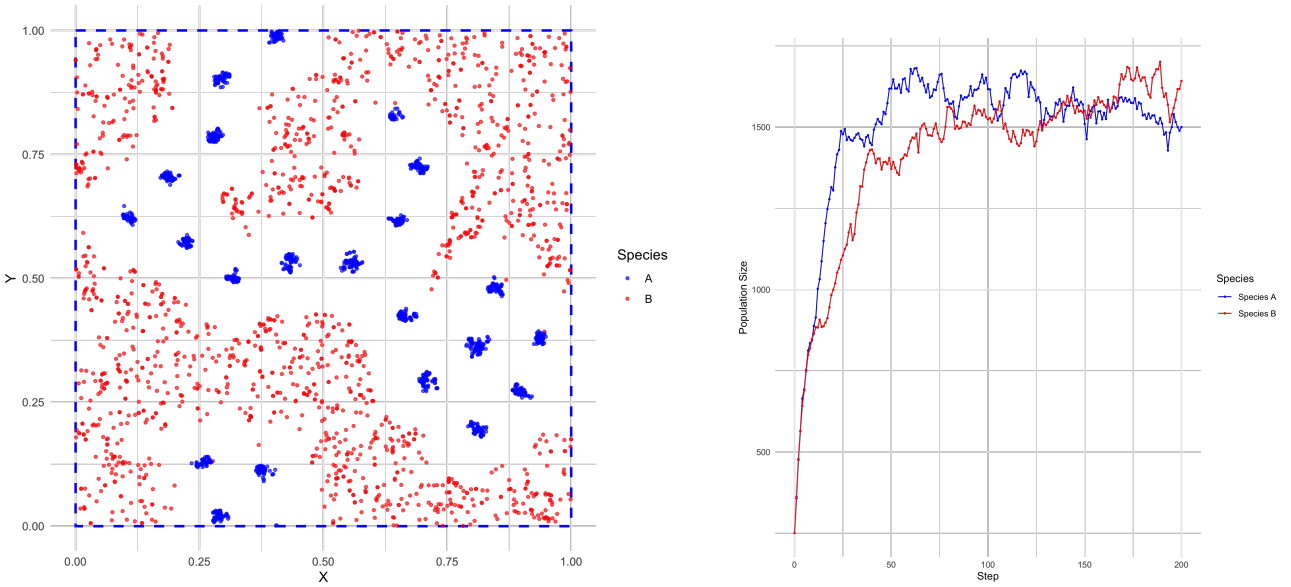

(a) (b)

Figure 5.15: Competition between Brownian ($\mu_A = 5$) and Lévy ($\mu_B = 1.5$) walkers with an increased base birth rate $r_{\mathrm{b}}^0 = 2$ and no motility effects. (a) Final spatial configuration after 200 steps. (b) Population dynamics over time ending with $N_A = 1500$ and $N_B = 1642$. The higher birth rate allows Brownian walkers to survive despite the Lévy walkers' exploratory advantage.

Figure 5.15a shows that with $r_{\mathrm{b}}^0 = 2$, Brownian clusters become more resilient, acting like strongholds that can maintain their populations even when surrounded by Lévy walkers. There we can see the distinct "death zones" form between clusters (in this case between species). These areas occur where competition from both species overlaps most intensely, leading to conditions where:

$$r_b^i \to 0 \qquad \text{(reproduction suppressed)}$$
$$r_d^i \gg r_d^0 \qquad \text{(mortality increased)}$$

These sharp boundaries illustrate how local competition shapes the environment into separate territories divided by inhospitable zones.

The population dynamics in Figure 5.15b display oscillatory behavior that qualitatively resembles predator-prey cycles, though they are driven solely by competition and movement, rather than predation. The cycle seem to go through the following stages:

1. *Brownian expansion*: In regions with low Lévy walker density, Brownian walkers reproduce rapidly, forming dense clusters. Their high birth rate allows them to grow rapidly, trying to reach the maximum number of individuals allowed by local competition. This

limitation comes from intraspecific competition (controlled by β as $\alpha = 0$) and interspecific pressure from nearby Lévy walkers (through κ_b and κ_d).

2. *Lévy incursion*: As Brownian clusters try to stabilize, Lévy walkers, thanks to their long-range movement, occasionally jump into these areas. Their unpredictable arrivals increase competition between the two species.

3. *Competitive suppression*: The presence of Lévy walkers near Brownian clusters reduces the Brownian birth rate (via $\kappa_b \hat{N}_R^{A,i}$) and increases their death rate (via $\kappa_d \hat{N}_R^{A,i}$). This interspecific pressure causes Brownian populations to decline, often dropping below earlier levels.

4. *Lévy dispersal or death, and Brownian recovery*: As the number of Brownian walkers falls, local competition decreases. Lévy walkers either move away in search of new regions or die off, further easing the pressure. This creates an opportunity for Brownian clusters to recover and grow again toward their equilibrium size.

These oscillations are driven by delayed feedback. Once Brownian clusters are formed, the Lévy walkers that may appear increase competition and cause Brownian decline. Only after Lévy walkers disperse or die does the environment become favorable again, allowing Brownian populations to rebound. Crucially, Brownian walkers avoid extinction because of their high intrinsic birth rate r_{b0} we imposed, which enables this repeated cycle of collapse and recovery.

5.4.3.2 Lévy vs. Lévy Walkers: Results and Observations

Having explored how clustering strategies like Brownian motion can either coexist with or be overpowered by Lévy explorers, we now turn to Lévy walkers competing against each other. Here, both species rely on long-range exploratory movement, but with slightly different step length exponents, species A with $\mu_A = 2$ and species B with $\mu_B = 1.5$.

Even though they share the same movement style, the difference in μ still creates a competitive imbalance. As we have seen before, a lower μ means more frequent long jumps, allowing those walkers to better explore and occupy new territory. That small shift gives species B a notable edge.

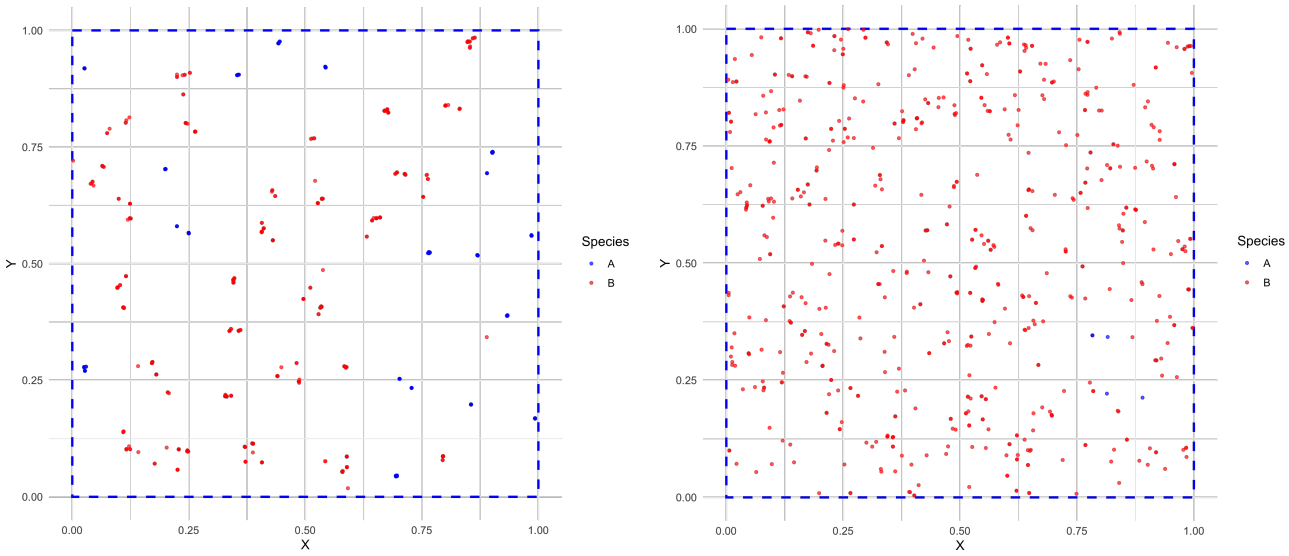

(a) Step: 59, $N_A = 305$, $N_B = 503$

(b) Step: 59, $N_A = 5$, $N_B = 605$

Figure 5.16: Competition between Lévy walkers ($\mu_A = 2$ vs $\mu_B = 1.5$). Left: motility effects maintains coexistence with B dominating. Right: without motility effects, A approaches extinction by step 59. The species with lower μ (more long jumps) consistently dominates.

Figure 5.16b shows what happens when motility effects are removed. Just like in the Lévy vs. Brownian case, the lack of spatial self-organization allows the more mobile species (B) to dominate rapidly. By step 59, species A is practically extinguished, with only 5 walkers remaining. This outcome is consistent with the idea that higher motility offers a competitive edge when spatial self-organization is suppressed for the given conditions.

As seen before, when the base birth rate is low ($r_{\mathrm{b}}^0 = 0.5$), clustering alone is not enough to survive. Without motility effects, forming tight groups does not help and it actually makes things worse by increasing exposure to interspecies competition.

In contrast, in Figure 5.16a, we can clearly see how motility effects changes the outcome. Species A manages to form stable clusters that hold their ground despite the motility advantage of species B. Spatial segregation and reduced overlap between species lower interspecific competition at the boundaries, enabling both species to coexist.

Finally, Figure 5.17 shows that the dynamics extend beyond early competition. These simulations were deliberately run for 300 steps to capture long-term behavior beyond initial transients. When motility effects are present, we observe sustained coexistence even at step 300, with both species maintaining strong populations due to spatial segregation (panel (a)).

Interestingly, the presence of motility regulation also leads to population oscillations that qualitatively resemble predator-prey cycles (panel (b)), similar to those observed earlier. These oscillations emerge purely from movement and competitive interactions, underscoring the complex dynamics that can arise from motility-mediated self-organization.

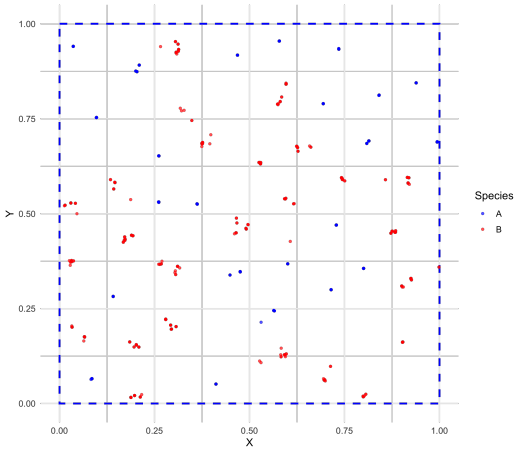

(a) Step: 300, $N_A = 425$, $N_B = 462$

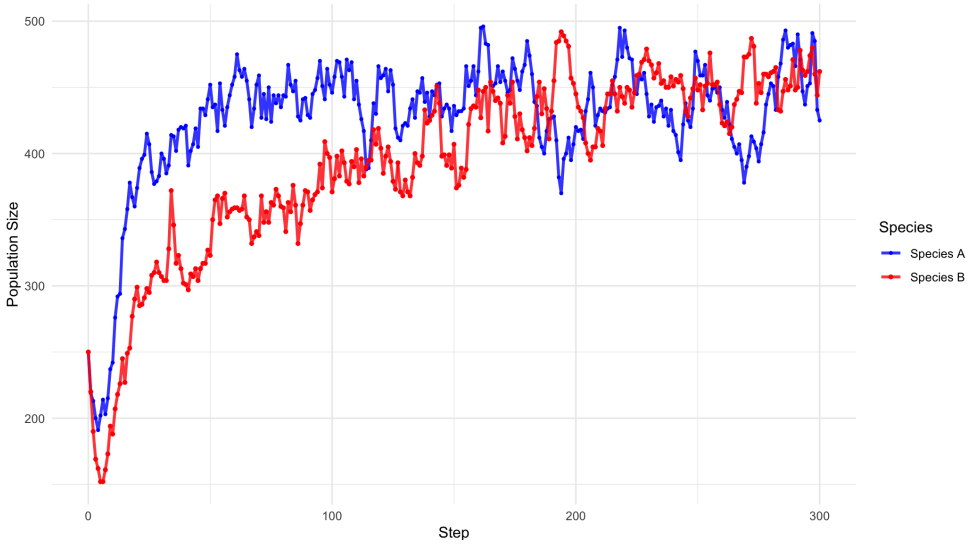

(b)

Figure 5.17: Long-term competition between Lévy walkers ($\mu_A = 2$ vs $\mu_B = 1.5$). (a) Sustained coexistence with motility effects at step 300. (b) Oscillatory dynamics with motility effects in the population vs steps graph.

Chapter 6

Conclusions

This work examined how Lévy flight movement strategies influence ecological dynamics, from individual foraging to interspecies competition, using analytical reasoning and numerical simulations. Our findings demonstrate that movement alone, governed by simple rules, is a key factor in shaping spatial patterns and species interactions.

In one-dimensional foraging, search efficiency depends on both the movement mode and the metric used. Destructive foraging favors long jumps (low μ), while non-destructive foraging performs better near $\mu \approx 2$. Efficiency measures vary with how they are evaluated, indicating the need for careful interpretation.

In two-dimensional systems, spatial clustering arises through two main mechanisms. First, local birth-death dynamics in the bugs model lead to clusters separated by low-density "death zones." Second, motility-induced phase separation (MIPS) occurs when individuals slow down and become self-trapped in crowded regions. In both cases, movement patterns, interaction strength, and interaction range play key roles in shaping the resulting spatial structures.
Crucially, our study shows that motility regulation enables coexistence between competing species with different movement strategies. Without regulation, fast-moving Lévy walkers tend to dominate by occupying space rapidly. When individuals adjust their speed based on local neighbors, spatial segregation and stable coexistence emerge, often with increased total populations. Oscillatory population cycles and sharp spatial boundaries arise naturally from these minimal ingredients of movement and local interaction.

Our objective was to understand how Lévy flight strategies affect species competition and spatial patterns. The results confirm that differences in motility and competition indeed give rise to rich spatial self-organization and coexistence dynamics, fulfilling our research goal.

6.1 Theoretical and Practical Implications

From a theoretical perspective, this work contributes to the broader understanding of how spatial self-organization can arise in ecological systems. It supports the idea that movement, when coupled with simple local rules, is sufficient to produce complex and structured behaviors. Practically, our results have potential applications in diverse fields. In ecology and conservation, they provide insights into species dispersal and coexistence. In epidemiology, understanding how movement modulates interactions can inform models of disease spread.

6.2 Limitations and Further Research

Despite its insights, this study has limitations. Foraging efficiency was analyzed only in one dimension and was not compared systematically with other strategies such as Gaussian walks. The competition models assumed symmetric species parameters, leaving open questions about how differences in interaction range, reproduction, or motility might shift outcomes. Results may also be sensitive to initial conditions and parameter values, so more extensive averaging would strengthen robustness.

Periodic boundary conditions, while computationally efficient, may distort long-range movement effects. Lévy walkers crossing a domain reappear on the other side, which may reduce the ecological impact of large jumps. Future work could test alternative boundary conditions, such as absorbing or reflective edges, to explore spatial confinement and edge effects more realistically.

Further directions include studying heterogeneous environments to test the generality of observed mechanisms, introducing asymmetries in species traits, or allowing movement strategies to evolve. Finally, combining simulations with analytical tools would clarify the mechanisms behind phase transitions between exclusion, coexistence, and pattern formation.

In summary, Lévy flights are not only efficient search strategies but also fundamental drivers of ecological structure and diversity. Motility regulation emerges as a key factor in enabling coexistence and spatial self-organization, revealing the deep link between movement and life.

Personal Thoughts

Developing this project has been a rewarding journey through mathematical modeling, computational problem-solving, and biological insight. Implementing the simulations in R taught me valuable lessons about balancing computational efficiency with model complexity, especially when managing thousands of interacting agents in two-dimensional space. Visualizations played a key role, not only in building intuition but also in debugging, turning abstract equations into observable and understandable dynamics.

Some of the most exciting moments came from unexpected findings. Observing oscillations emerge from the competition model (Figure 5.17) was a clear highlight. Similarly, seeing "death zones" appear spontaneously between competing species (Figure 5.15) demonstrated how simple local rules can generate large-scale spatial organization. That said, I especially enjoyed working on the initial stages of pattern formation, those first emerging structures were the most satisfying to explore.

Several challenges helped me grow as a problem-solver. In the 1D foraging models, the differences between my efficiency results and those found in the literature led me to deeply rethink what was actually being measured. In 2D simulations, defining appropriate stabilization thresholds and identifying relevant parameter regimes required careful, systematic exploration. Here, using the mean-field approximation to get a first idea of how the system behaves has proved essential. I first encountered this approach during the Interdisciplinary Seminars, where working with a research group introduced me to structured scientific reasoning. That experience had a lasting impact, showing me how to build a coherent research process and helping me stay organized and focused throughout this project.

In addition, several core subjects provided crucial foundations. Statistics, combinatorics and probability, statistical mechanics, and mathematical analysis all contributed directly to my ability to design, interpret, and refine the models. These subjects shaped the way I approach complex problems and were indispensable throughout the entire project.

Looking ahead, I would like to explore the following directions:

- *Evolutionary dynamics*: Allowing the movement exponent μ to evolve over time could uncover optimal strategies under competitive pressure.
- *Resource gradients*: Introducing heterogeneous landscapes would bring the model closer to ecological realism.
- *Boundary conditions*: Exploring alternative boundary types such as absorbing or reflective edges could reveal how spatial confinement affects coexistence and movement strategies.
- *Experimental validation*: Collaborating with microbiologists to test predictions in microbial competition assays would be an exciting bridge between theory and experiment.

This project transformed my understanding of biological motion. What appears as simple random movement can actually drive the emergence of intricate patterns and stable coexistence between species that might otherwise outcompete one another. This experience deepened my appreciation for how mathematics reveals nature's underlying order.

Analysis of Ethical and Social Responsibility

This project, focused on the ecological effects of movement strategies like Lévy flights, primarily lies within the domain of theoretical ecology and computational modeling. However, even in abstract scientific work, it is important to reflect on its broader ethical and social implications.

Gender Equality

The project does not involve human subjects, user interfaces, or social data, so it does not directly relate to gender issues or risk incorporating gender bias. Code and documentation were written in neutral terms.

Environmental Sustainability

Although the study is theoretical, it deals with ecological systems and mechanisms that can affect biodiversity and coexistence. By modeling how simple movement rules promote or hinder species coexistence, the project contributes to a better understanding of spatial dynamics in ecosystems, which may be relevant in contexts such as conservation planning or ecosystem management.

Social Responsibility

The models developed here do not involve human populations, social systems, or applications with direct societal impact. However, the methodology adheres to open science principles, using reproducible code and open-source tools. In that sense, the work contributes to good scientific practices and knowledge sharing.

Ethics

The work was conducted in accordance with ethical standards for computational research. No biological experiments were performed, and all simulations were carried out transparently. Results were interpreted cautiously and all sources and tools used were properly cited. There are no foreseeable negative ethical implications from the content or methodology of this project.

References

[1] Aleix Casals. Code repository for lévy flights project. https://github.com/AleixCaCh/levy-flights-project.git, 2025. Accessed: June 2025.

[2] Michael E. Cates and Julien Tailleur. Motility-induced phase separation. *Annual Review of Condensed Matter Physics*, 6:219–244, 2015.

[3] Emilio Hernández-García, Els Heinsalu, and Cristóbal López. Spatial patterns of competing random walkers. *Ecological Complexity*, 21:166–176, March 2015.

[4] H. Paul Keeler. The inverse method for simulating random variables, 2015. Accessed: 2025-05-05.

[5] P. Pirolli and S. K. Card. Information foraging. *Psychological Review*, 106(4):643–675, 1999.

[6] G.M Viswanathan, V Afanasyev, Sergey V Buldyrev, Shlomo Havlin, M.G.E da Luz, E.P Raposo, and H.Eugene Stanley. Lévy flights in random searches. *Physica A: Statistical Mechanics and its Applications*, 282(1):1–12, 2000.

[7] Wikipedia contributors. Active matter, 2024. Accessed: 2025-05-04.

Appendix A

Mathematical Derivations

A.1 1st and 2nd Moment of the Lévy Flights PDF

Now let's study the first moment, also known as the expected value of $p(\ell)$ for $\mu > 1$. We will compute

$$< \ell > = \int_{\ell_{min}}^{+\infty} l \cdot p(l) dl$$

and see if it gives a finite value or if it diverges.

- For $\mu > 2$

$$\begin{aligned} < \ell > &= \int_{\ell_{\min}}^{+\infty} l \cdot C \cdot l^{-\mu} \, dl \\ &\Rightarrow \int_{\ell_{\min}}^{+\infty} C \cdot l^{-\mu+1} \, dl = C \int_{\ell_{\min}}^{+\infty} l^{-\mu+1} \, dl \\ &= C \left. \frac{l^{2-\mu}}{2-\mu} \right|_{\ell_{\min}}^{+\infty} \\ &= C \left(\lim_{l \to +\infty} \frac{l^{2-\mu}}{2-\mu} - \frac{\ell_{\min}^{2-\mu}}{2-\mu} \right) \\ &= \boxed{C \cdot \frac{\ell_{\min}^{2-\mu}}{\mu - 2}} \end{aligned}$$

In the evaluation of the anti-derivative, the term at the upper limit is

$$\lim_{l \to +\infty} \frac{l^{2-\mu}}{2-\mu} = 0$$

Since $\mu > 2 \to 2 - \mu < 0$ in this range, we are taking the limit of a negative power of l, which vanishes as $l \to +\infty$. Therefore, the integral converges and we have a well-defined

expected value, i.e., it is a finite real value.

- For $\mu = 2$

$$\begin{aligned} < \ell > &= \int_{\ell_{\min}}^{+\infty} l \cdot C \cdot l^{-2}\, dl \\ &\Rightarrow \int_{\ell_{\min}}^{+\infty} C \cdot l^{-1}\, dl = C \int_{\ell_{\min}}^{+\infty} \frac{1}{l}\, dl \\ &= C \ln(l)|_{\ell_{\min}}^{+\infty} \\ &= C \left(\lim_{l \to +\infty} \ln(l) - \ln(\ell_{\min}) \right) \\ &= C \cdot (+\infty - \ln(\ell_{\min})) = +\infty \end{aligned}$$

As we can see, the integral diverges for $\mu = 2$ due to the logarithmic term growing without bound. This means that the probability density function has a divergent expected value.

- For $\mu < 2$

$$\begin{aligned} < \ell > &= \int_{\ell_{\min}}^{+\infty} l \cdot C \cdot l^{-\mu}\, dl \\ &\Rightarrow \int_{\ell_{\min}}^{+\infty} C \cdot l^{-\mu+1}\, dl = C \int_{\ell_{\min}}^{+\infty} l^{-\mu+1}\, dl \\ &= C \left. \frac{l^{2-\mu}}{2-\mu} \right|_{\ell_{\min}}^{+\infty} \\ &= C \left(\lim_{l \to +\infty} \frac{l^{2-\mu}}{2-\mu} - \frac{\ell_{\min}^{2-\mu}}{2-\mu} \right) \\ &= C \left(+\infty - \frac{\ell_{\min}^{2-\mu}}{2-\mu} \right) = +\infty \end{aligned}$$

Again, the integral diverges for $\mu < 2$ because in this regime the exponent $2 - \mu > 0$, so $l^{2-\mu}$ grows without bound as $l \to +\infty$. As a result, we do not have a well defined first moment.

We proceed with study the second moment, also known as the variance of $p(\ell)$ for $\mu > 1$. We will compute

$$< \ell^2 > = \int_{\ell_{min}}^{+\infty} l^2 \cdot p(l) dl$$

and see if it gives a finite value or if it diverges.

- For $\mu > 3$

$$\begin{aligned} < \ell^2 > &= \int_{\ell_{\min}}^{+\infty} l^2 \cdot C \cdot l^{-\mu}\, dl \\ &\Rightarrow \int_{\ell_{\min}}^{+\infty} C \cdot l^{-\mu+2}\, dl = C \int_{\ell_{\min}}^{+\infty} l^{-\mu+2}\, dl \\ &= C\, \frac{l^{3-\mu}}{3-\mu}\bigg|_{\ell_{\min}}^{+\infty} \\ &= C \left(\lim_{l \to +\infty} \frac{l^{3-\mu}}{3-\mu} - \frac{\ell_{\min}^{3-\mu}}{3-\mu} \right) \\ &= \boxed{C \cdot \frac{\ell_{\min}^{3-\mu}}{\mu - 3}} \end{aligned}$$

In the evaluation of the anti-derivative, the term at the upper limit is

$$\lim_{l \to +\infty} \frac{l^{3-\mu}}{3-\mu} = 0$$

Since $\mu > 3 \to 3 - \mu < 0$ in this range, we are taking the limit of a negative power of l, which vanishes as $l \to +\infty$. Therefore, the integral converges and we have a well-defined variance.

- For $\mu = 3$

$$\begin{aligned} < \ell^2 > &= \int_{\ell_{\min}}^{+\infty} l^2 \cdot C \cdot l^{-3}\, dl \\ &\Rightarrow \int_{\ell_{\min}}^{+\infty} C \cdot l^{-1}\, dl = C \int_{\ell_{\min}}^{+\infty} \frac{1}{l}\, dl \\ &= C\, \ln(l)|_{\ell_{\min}}^{+\infty} \\ &= C \left(\lim_{l \to +\infty} \ln(l) - \ln(\ell_{\min}) \right) \\ &= C\, (+\infty - \ln(\ell_{\min})) = +\infty \end{aligned}$$

As we can see, the integral diverges for $\mu = 3$ due to the logarithmic term growing without bound. This means that the probability density function has a divergent variance.

- For $\mu < 3$

$$
\begin{aligned}
< \ell^2 > &= \int_{\ell_{\min}}^{+\infty} l^2 \cdot C \cdot l^{-\mu}\, dl \\
&\Rightarrow \int_{\ell_{\min}}^{+\infty} C \cdot l^{-\mu+2}\, dl = C \int_{\ell_{\min}}^{+\infty} l^{-\mu+2}\, dl \\
&= C \left. \frac{l^{3-\mu}}{3-\mu} \right|_{\ell_{\min}}^{+\infty} \\
&= C \left(\lim_{l \to +\infty} \frac{l^{3-\mu}}{3-\mu} - \frac{\ell_{\min}^{3-\mu}}{3-\mu} \right) \\
&= C \left(+\infty - \frac{\ell_{\min}^{3-\mu}}{3-\mu} \right) = +\infty
\end{aligned}
$$

  Again, the integral diverges for $\mu < 3$ because in this regime the exponent $3 - \mu > 0$, so $l^{3-\mu}$ grows without bound as $l \to +\infty$. As a result, we do not have a well defined second moment.

A.2 Expression for N in 1D Brownian Random Walk

We shall show that in the specific case of a 1D Brownian random walk where all steps have a fixed length r_v (corresponding to $\mu > 3$ on the Lévy flight probability distribution), the resulting expression is $N = x(L - x)r_v^{-2}$.

Let $N(x)$ denote the expected number of steps needed to reach a target site, starting from position x. We assume there are two target sites: one at $x = 0$ and another at $x = L$. Since the walker can only jump a fixed distance r_v either to the left or to the right, the process satisfies the following recurrence relation:

$$
N(x) = \begin{cases} 0 & \text{if } x = 0 \text{ or } x = L, \\ 1 + \frac{1}{2}N(x - r_v) + \frac{1}{2}N(x + r_v) & \text{if } x \in (0, L). \end{cases}
$$

Here, the walker has a 50% chance of jumping to the right (to position $x + r_v$) and a 50% chance of jumping to the left (to $x - r_v$). We add 1 in the recursive case because whenever the walker is not yet at a target it will do one step. At the boundaries $x = 0$ and $x = L$, no further steps are needed, which justifies the value 0 in those cases.

To solve the recurrence relation, we consider the discrete positions $x = kr_v$, where $k = 0, 1, 2, \ldots, n$ and $L = nr_v$ for some positive integer n. Define $N_k = N(k) = N(x)$ at $x = kr_v$. Then the recurrence relation becomes:

$$N_k = 1 + \frac{1}{2}N_{k-1} + \frac{1}{2}N_{k+1}, \quad \text{for } 1 \leq k \leq n-1,$$

with boundary conditions:

$$N_0 = N_n = 0.$$

This is a linear second-order difference equation with constant coefficients. We propose the following expression for the homogenous part:

$$N_k = A^k,$$

Substituting into the recurrence:

$$N_{k+1} - 2N_k + N_{k-1} = 0 \rightarrow A^{k-1} \cdot (A^2 - 2A + 1) = 0 \rightarrow (A-1)^2 = 0$$

Which means that $A = 1$ is a double root, hence:

$$N_h(k) = B \cdot 1^k + C \cdot 1^k k = B + C \cdot k$$

Now we find a particular solution of the form

$$N_p(k) = Dk^2,$$

since the inhomogeneous term on the right-hand side of the recurrence is constant (equal to 1). Substituting $N_p(k) = Dk^2$ into the recurrence relation:

$$N_k = 1 + \frac{1}{2}N_{k-1} + \frac{1}{2}N_{k+1},$$

we compute:

$$\text{LHS: } N_k = Dk^2,$$

$$\begin{aligned}\text{RHS: } 1 + \frac{1}{2}D(k-1)^2 + \frac{1}{2}D(k+1)^2 &= 1 + \frac{D}{2}\left(k^2 - 2k + 1\right) + \frac{D}{2}\left(k^2 + 2k + 1\right) \\ &= 1 + \frac{D}{2}(2k^2 + 2) = 1 + Dk^2 + D.\end{aligned}$$

So:

$$Dk^2 = 1 + Dk^2 + D \Rightarrow 0 = 1 + D \Rightarrow D = -1.$$

Therefore, a particular solution is:

$$N_p(k) = -k^2.$$

The general solution is then the sum of the homogeneous and particular parts:

$$N_k = N_h(k) + N_p(k) = B + Ck - k^2.$$

Now we apply the boundary conditions $N_0 = 0$ and $N_n = 0$ to determine B and C:

$$\begin{aligned} N_0 &= B + C \cdot 0 - 0^2 = B = 0, \\ N_n &= 0 = B + Cn - n^2 = Cn - n^2 \Rightarrow C = n. \end{aligned}$$

So the complete solution becomes:

$$N_k = nk - k^2 = k(n - k).$$

Returning to the original continuous variable $x = kr_v$, and noting $n = \frac{L}{r_v}$, we substitute:

$$N(x) = N_k = \frac{x}{r_v}\left(\frac{L}{r_v} - \frac{x}{r_v}\right) = \frac{x(L-x)}{r_v^2}.$$

$$\boxed{N(x) = \frac{x(L-x)}{r_v^2}} \tag{A.1}$$

This quadratic form shows that the expected number of steps is zero at the boundaries and maximal at the midpoint $x = \frac{L}{2}$, which aligns with physical intuition for a symmetric 1D random walk.

A.3 Efficiency Derivation for Destructive and Nondestructive Foraging

We start deriving the expression for the efficiency at $\mu = 2$ for both destructive and nondestructive foraging, under the assumptions already discussed.

Recall that targets are located exactly at distance λ, and we are in the regime where $\lambda \gg r_v = l_{\min}$.

Since equation 3.4 is not valid for $\mu = 2$, we begin by computing the mean step length directly. Note that in this case, the normalization constant is:

$$C = \frac{\mu - 1}{l_{\min}^{1-\mu}} = r_v$$

The mean step length is given by:

$$\begin{aligned}\langle \ell \rangle &= \int_{r_v}^{+\infty} l \cdot p(l)\, dl = \int_{r_v}^{+\infty} l \cdot C \cdot l^{-\mu}\, dl \\ &= \int_{r_v}^{\lambda} l \cdot C \cdot l^{-\mu}\, dl + \int_{\lambda}^{+\infty} l \cdot C \cdot l^{-\mu}\, dl\end{aligned}$$

Then, as explained earlier, we approximate the second integral by treating all steps beyond λ as exactly of length λ, since targets are only located at this distance.

$$\begin{aligned}\langle \ell \rangle &\approx C \left(\int_{r_v}^{\lambda} l^{1-\mu}\, dl + \lambda \int_{\lambda}^{+\infty} l^{-\mu}\, dl \right) = C \left(\int_{r_v}^{\lambda} l^{-1}\, dl + \lambda \int_{\lambda}^{+\infty} l^{-2}\, dl \right) \\ &= r_v \left[\ln(\lambda) - \ln(r_v) \right] + \lambda r_v \cdot \lambda^{-1} = r_v \left[\ln\left(\frac{\lambda}{r_v} \right) + 1 \right]\end{aligned}$$

Now, we compute the efficiency $\eta = 1/(N \cdot \langle \ell \rangle)$ for each case. Starting with destructive foraging:

$$\begin{aligned}\eta_d &= \frac{1}{N_d \cdot \langle \ell \rangle} = \frac{1}{K \left(\frac{\lambda}{r_v} \right)^{\mu-1} \cdot r_v \left[\ln\left(\frac{\lambda}{r_v} \right) + 1 \right]} = \frac{1}{K \left(\frac{\lambda}{r_v} \right) \cdot r_v \left[\ln\left(\frac{\lambda}{r_v} \right) + 1 \right]} \\ &= \frac{1}{K\lambda \left[\ln\left(\frac{\lambda}{r_v} \right) + 1 \right]}\end{aligned}$$

Now with nondestructive foraging:

$$\eta_n = \frac{1}{N_n \cdot \langle \ell \rangle} = \frac{1}{K\left(\frac{\lambda}{r_v}\right)^{(\mu-1)/2} \cdot r_v \left[\ln\left(\frac{\lambda}{r_v}\right) + 1\right]} = \frac{1}{K\left(\frac{\lambda}{r_v}\right)^{1/2} \cdot r_v \left[\ln\left(\frac{\lambda}{r_v}\right) + 1\right]}$$
$$= \frac{1}{K\sqrt{\lambda r_v}\left[\ln\left(\frac{\lambda}{r_v}\right) + 1\right]}$$

We now turn our attention to the case where $2 < \mu \leq 3$, which requires a separate analysis. Note that in this case, $2-\mu < 0$, therefore, $\lambda^{2-\mu} - r_v^{2-\mu} \approx -r_v^{2-\mu}$ when $\lambda >> r_v$ as $\lambda^{-n} << r_v^{-n}$ for some positive n. Then, proceeding with the destructive foraging:

$$\eta_d = \frac{1}{N_d \cdot < \ell >} = \frac{1}{K\lambda^{\mu-1} \cdot \left[\left(\frac{\mu-1}{2-\mu}\right)\left(\lambda^{2-\mu} - r_v^{2-\mu}\right) + \lambda^{2-\mu}\right]}$$
$$\approx \frac{1}{K\lambda^{\mu-1} \cdot \left[\left(\frac{\mu-1}{\mu-2}\right) r_v^{2-\mu} + \lambda^{2-\mu}\right]} = \frac{\mu-2}{K\lambda^{\mu-1} \cdot \left[(\mu-1) r_v^{2-\mu} + (\mu-2)\lambda^{2-\mu}\right]}$$
$$= \frac{\mu-2}{K\lambda^{\mu-1}\ r_v^{2-\mu} \cdot (\mu-1)} = \frac{\mu-2}{K\lambda \cdot (\mu-1)}\left(\frac{r_v}{\lambda}\right)^{\mu-2}$$

Proceeding similarly for the nondestructive foraging:

$$\eta_n = \frac{1}{N_n \cdot < \ell >} = \frac{1}{K\left(\frac{\lambda}{r_v}\right)^{(\mu-1)/2} \cdot \left[\left(\frac{\mu-1}{2-\mu}\right)\left(\frac{\lambda^{2-\mu} - r_v^{2-\mu}}{r_v^{1-\mu}}\right) + \frac{\lambda^{2-\mu}}{r_v^{1-\mu}}\right]}$$
$$\approx \frac{1}{K\lambda^{(\mu-1)/2}\ r_v^{(1-\mu)/2} \cdot r_v^{\mu-1}\left[\left(\frac{\mu-1}{\mu-2}\right) r_v^{2-\mu} + \lambda^{2-\mu}\right]}$$
$$= \frac{\mu-2}{K\lambda^{(\mu-1)/2}\ r_v^{(1-\mu)/2} \cdot r_v^{\mu-1}\left[(\mu-1) r_v^{2-\mu} + (\mu-2)\lambda^{2-\mu}\right]}$$
$$\approx \frac{\mu-2}{K\lambda^{(\mu-1)/2}\ r_v^{(1-\mu)/2} \cdot r_v^{\mu-1}(\mu-1) r_v^{2-\mu}} = \frac{\mu-2}{K\lambda^{(\mu-1)/2}\ r_v^{(1-\mu)/2}(\mu-1) r_v}$$
$$= \frac{\mu-2}{K r_v(\mu-1)}\left(\frac{r_v}{\lambda}\right)^{(\mu-1)/2}$$

In this way, we obtain the efficiency expressions given in eqs. (3.8) and (3.11).

A.4 Mean-Field Theory Derivation for Competitive Bugs in Dynamic Stabilization

We derive the mean-field equilibrium for the two-species competition model defined by the birth and death rates introduced in Section 5.4:

$$r_{\mathrm{b}}^{i} = \max\left(0, r_{\mathrm{b}}^{0} - \alpha N_R^i - \kappa_b \hat{N}_R^i\right), \quad r_{\mathrm{d}}^{i} = r_{\mathrm{d}}^{0} + \beta N_R^i + \kappa_d \hat{N}_R^i \tag{A.2}$$

First, recall that the Mean-Field Approximation assumes:

1. **Spatial homogeneity**: Individuals are uniformly distributed, so local densities are equal to global averages.
2. **Equilibrium condition**: Birth and death rates balance for each species.

To apply the mean-field approach to this two-species competition, we consider the average number of neighbors of each species around a typical individual. Since individuals interact locally, but we assume spatial homogeneity, the local neighborhood composition can be approximated by global average densities.

Specifically, for species A and B, we define:

- N_R^A: The average number of neighbors belonging to species A around any individual (whether species A or B).
- N_R^B: The average number of neighbors belonging to species B around any individual.

These quantities represent the expected local crowding from each species that impacts the birth and death rates via competition.

Assuming both species share the same intrinsic parameters $(r_b^0, r_d^0, \alpha, \beta, \kappa_b, \kappa_d)$, we write the mean birth and death rates for each species as functions of these average neighbor counts.

For species A:

$$r_b^A = r_b^0 - \alpha N_R^A - \kappa_b N_R^B, \tag{A.3}$$
$$r_d^A = r_d^0 + \beta N_R^A + \kappa_d N_R^B. \tag{A.4}$$

Similarly, for species B:

$$r_b^B = r_b^0 - \alpha N_R^B - \kappa_b N_R^A, \tag{A.5}$$
$$r_d^B = r_d^0 + \beta N_R^B + \kappa_d N_R^A. \tag{A.6}$$

At equilibrium, the average birth and death rates for each species must be equal:

$$r_b^A = r_d^A, \tag{A.7}$$
$$r_b^B = r_d^B. \tag{A.8}$$

Substituting from (A.3) and (A.4) into (A.7), and from (A.5) and (A.6) into (A.8), we get the system:

$$r_b^0 - \alpha N_R^A - \kappa_b N_R^B = r_d^0 + \beta N_R^A + \kappa_d N_R^B, \tag{A.9}$$
$$r_b^0 - \alpha N_R^B - \kappa_b N_R^A = r_d^0 + \beta N_R^B + \kappa_d N_R^A. \tag{A.10}$$

Rearranging each equation to isolate terms:

$$r_b^0 - r_d^0 = (\alpha + \beta) N_R^A + (\kappa_b + \kappa_d) N_R^B, \tag{A.11}$$
$$r_b^0 - r_d^0 = (\alpha + \beta) N_R^B + (\kappa_b + \kappa_d) N_R^A. \tag{A.12}$$

Now solving for N_R^A and N_R^B let

$$\Delta r := r_b^0 - r_d^0, \quad a := \alpha + \beta, \quad k := \kappa_b + \kappa_d.$$

Then the system (A.11) and (A.12) becomes:

$$\Delta r = a N_R^A + k N_R^B, \tag{A.13}$$
$$\Delta r = a N_R^B + k N_R^A. \tag{A.14}$$

Subtracting (A.14) from (A.13) gives:

$$0 = a(N_R^A - N_R^B) - k(N_R^A - N_R^B) = (a - k)(N_R^A - N_R^B).$$

This yields two cases:

- If $a \neq k$, then $N_R^A = N_R^B$.
- If $a = k$, the equations are symmetric so we cannot determine the difference between N_R^A and N_R^B.

Then, defining $N_R := N_R^A = N_R^B$ and assuming $a \neq k$, we substitute into (A.13) and obtain:

$$\Delta r = a N_R + k N_R = (a + k) N_R.$$

Therefore,

$$N_R = \frac{\Delta r}{a+k} = \frac{r_b^0 - r_d^0}{\alpha + \beta + \kappa_b + \kappa_d}.$$

This expression shows that as long as $r_b^0 - r_d^0 \neq 0$, the system admits a non-trivial equilibrium with coexistence of both species.